New insights into the nucleation of portlandite and the effects of polymeric additives

Benjamin Madeja, Denis Gebauer, Maximilian Marsiske, Andreas Ott, Markus Rückel, Annet Baken, Tomasz Stawski, Alejandro Fernandez-Martinez, Alexander E.S. van Driessche, Helmut Cölfen, et al.

New Insights into the Nucleation of Portlandite and the Effects of Polymeric Additives

*Benjamin Madeja,[1] Denis Gebauer,[2] Maximilian R. Marsiske,[1] Andreas Ott,[3] Markus Rückel,[3] Annet Baken,[4,6] Tomasz M. Stawski,[5] Alejandro Fernandez-Martinez,[6] Alexander E. S. Van Driessche,[6,7] Helmut Cölfen[1] and Matthias Kellermeier[3]**

[1]Physical Chemistry, University of Konstanz, Universitätsstraße 10, D-78457 Konstanz, Germany.

[2]Institute of Inorganic Chemistry, Leibniz University Hannover, Callinstraße 9, 30167 Hannover, Germany.

[3]Material Science, BASF SE, Carl-Bosch-Straße 38, D-67056 Ludwigshafen, Germany.

[4]ESRF – The European Synchrotron, 71 Avenue des Martyrs, F-38000 Grenoble, France.

[5]Materials Chemistry, Federal Institute for Materials and Testing (BAM), Richard-Willstätter-Straße 11, D-12489 Berlin, Germany.

[6]Univ. Grenoble Alpes, Univ. Savoie Mont Blanc, CNRS, IRD, IFSTTAR, ISTerre, F-38000 Grenoble, France.

[7]Instituto Andaluz de Ciencias de la Tierra (IACT), CSIC-University of Granada, E-18100 Armilla, Granada, Spain.

Keywords: Calcium hydroxide, nucleation, non-classical crystallization, mineralization, prenucleation clusters, amorphous precursors, polymer-controlled crystallization, potentiometric titration, cryo-TEM, SAXS, pair distribution function analysis, analytical ultracentrifugation.

Abstract: The crystallization of calcium hydroxide ($Ca(OH)_2$, CH, portlandite) is a key process during the early stages of cement hydration. In the present work, we have revisited the formation of this mineral through nucleation and growth from supersaturated aqueous solutions, in the light of the currently emerging picture of multistage "non-classical" crystallization. To that end, we developed a titration-based assay, in which stock solutions of both relevant ions are added simultaneously into a reservoir, where supersaturation increases slowly at constant stoichiometry until nucleation occurs. This procedure allows both pre- and early post-nucleation phenomena to be analyzed quantitatively. Complementarily, the early stages of portlandite mineralization were probed by various advanced characterization techniques, including cryo-transmission electron microscopy (cryo-TEM), in-situ small-angle X-ray scattering (SAXS), pair distribution function (PDF) analysis of high-energy X-ray scattering data, and analytical ultracentrifugation (AUC). The experimental data show that the formation of calcium hydroxide starts with the association of ions into clusters, which subsequently coalesce to form amorphous nanoparticles – much like what has been observed in the case of calcium carbonate and other prominent minerals. Subsequently, these particles aggregate and build networks, which eventually transform into hexagonal $Ca(OH)_2$ crystals. The presence of a soluble polycarboxylate – as a known inhibitor of portlandite crystallization – does not change the main characteristics of this multistep nucleation pathway, but it proved capable of significantly extending the lifetime of the amorphous intermediate phase and thus delaying the transition to the final crystalline phase. Our observations confirm the notion that "non-classical" crystallization is a much more common phenomenon than initially believed – and that, for minerals forming in aqueous environments, it may actually be the rule rather than the exception.

1. Introduction

A multitude of recent studies have shown that mineral formation can be far more complex than envisaged by classical models of nucleation and growth.[1,2] Instead of simple ion-by-ion association, the early stages of mineralization can involve – or rely on – the occurrence of larger precursors, which form on the basis of equilibrium thermodynamics. At some point in the supersaturated regime, the pre-nucleation equilibria are perturbed, and structural and/or dynamical changes may then lead to the aggregation of the precursors into more or less short-lived intermediate structures that will finally, upon stepwise transformation, yield a bulk crystalline phase.[3] The most prominent mineral investigated in this context is calcium carbonate, for which stable pre-nucleation clusters (PNCs), dense liquid-like phases, amorphous nanoparticles and metastable crystalline polymorphs were observed on the way from dissolved ions to rhombohedral calcite crystals.[4-8] Over the past few years, numerous pieces of (in)direct evidence have been collected suggesting that nucleation via multiple precursor and intermediate stages could be a common scenario for the crystallization of different types of inorganic minerals from aqueous solutions, including calcium phosphates,[9-11] calcium sulfate,[12-14] calcium oxalate,[15] calcium silicate hydrate,[16] and iron (oxyhydr)oxide.[17,18]

Calcium oxides and hydroxides are another class of interesting inorganic matter with great technological and industrial relevance. Both minerals are used for the production of construction materials[19] and fertilizers,[20] and play a key role in the Solvay process for soda production[21] and flue-gas desulfurization.[22] Consequently, their annual production is in the range of several hundred megatons.[23] Portlandite (i.e. crystalline $Ca(OH)_2$) is the second most abundant hydrated phase in Portland cements with low CaO content.[24] In cementitious systems, the formation of portlandite affects the hydration of other components like silicates or aluminates,[25] and

contributes to the mechanical properties of the final concrete.[26] Thus, detailed understanding of the mechanisms underlying the crystallization of portlandite bears great significance for large-scale industrial applications.

Early experimental studies on the homogeneous formation of calcium hydroxide from supersaturated aqueous solutions reported nucleation rates in the range of 10^3 cm^{-3} s^{-1}, which translated into critical cluster sizes of about 55 $Ca(OH)_2$ units according to classical nucleation theory.[27] In the past twenty years, most of the studies dealing with portlandite formation have indeed focused more on heterogeneous (re)crystallization phenomena using calcium oxide or calcium hydroxide ("slaked lime") as a starting material,[28-31] due to the relevance of such processes in lime-based mortars. For example, Rodriguez-Navarro et al. found that portlandite particles in aqueous dispersions experience significant changes when exposed to water for extended periods of time and/or upon drying, leading to the formation of well-defined nanoplatelets (as a result of dissolution-reprecipitation processes)[28] that subsequently may undergo irreversible oriented attachment during drying into colloidal superstructures, which account for the setting and stability of the dry hydrated lime.[29] Ageing of lime mortars (as well as other construction materials such as cements) is usually accompanied, either accidentally or on purpose, by carbonation and the formation of calcium carbonate polymorphs through dissolution and subsequent remineralization processes, which are often coupled and occur at or near the original portlandite/water interface.[32-34] Another interesting field of application, where heterogeneous portlandite (re)crystallization plays an important role, is the use of so-called "nanolimes" for the protection, repair and conservation of cultural heritage objects and structures.[35] Nanolimes are dispersions of $Ca(OH)_2$ particles in organic media (usually alcohols),

which are applied to paintings, stones, paper, wood and other substrates in order to achieve, upon carbonation, consolidation and/or deacidification of precious cultural objects.

Despite all these studies on portlandite formation and transformation under different practical settings, the actual mechanisms of $Ca(OH)_2$ nucleation from aqueous solution have not been elucidated in detail yet, especially concerning the possible occurrence of precursor and/or intermediates phases. Very recently, Rodriguez-Navarro et al.[36] extended their investigations on the portlandite system to conditions of homogeneous nucleation from solution and found that the formation of stable $Ca(OH)_2$ crystals is indeed preceded by multiple transient species and phases, including pre-nucleation clusters, dense liquid droplets, nanoparticles of amorphous calcium hydroxide (ACH), as well as a metastable nanocrystalline phase – a typical sequence of stages along increasing stability according to Ostwald's rule.[37] In the present work, we provide further compelling evidence corroborating this picture of "non-classical" portlandite crystallization. To this end, we have developed a titration-based assay, in which calcium and hydroxide ions are added simultaneously to a reservoir, in which solution speciation parameters are monitored continuously and supersaturation is slowly increased until precipitation takes place. During this process, the structural evolution in the system was probed using advanced characterization techniques such as in-situ small-angle X-ray scattering (SAXS) and pair-distribution function (PDF) analysis, cryo-transmission electron microscopy (cryo-TEM) and analytical ultracentrifugation (AUC). Finally, we investigated the influence of poly(acrylic acid) – as an archetype for polymer-controlled crystallization[38] – on the different stages of the newly discovered complex pathway of portlandite formation from solution.

2. Experimental Section

2.1 Reagents

All chemicals were of analytical grade and used without further purification. Calcium chloride dihydrate (≥99 %) and sodium hydroxide (≥99 %) were purchased from Sigma-Aldrich, while poly(acrylic acid) (PAA, M_w ≈ 6000 Da) was provided by BASF. Water was taken from a Milli-Q Direct 8 Water Purification System and subsequently boiled for 30 min to remove dissolved CO_2. The solvent and all prepared solutions were stored under an inert atmosphere to avoid recarbonation. For final washing of the precipitated portlandite particles during isolation, absolute-grade ethanol (Merck) was used.

2.2 Crystallization Experiments

Slow and controlled precipitation of portlandite was realized by simultaneous titration of $CaCl_2$ and NaOH stock solutions into a reservoir, in which multiple parameters were monitored to trace the progress of crystallization. For the titration experiments, an automated setup from Metrohm was used. The main operation unit was a 905 Titrando (Metrohm No. 2.905.0020) controlled by Tiamo 2.5 software, to which an 867 pH module (Metrohm No. 2.867.0010), an 856 conductivity module (Metrohm No. 2.856.0010), and two dosing units (800 Dosino, with 2 mL burettes, Metrohm No. 2.800.0010) were attached. To monitor the progress of the precipitation reaction, a turbidity probe (Optrode, Metrohm No. 6.1115.000) and a calcium ion-selective electrode (ISE, Metrohm No. 6.0510.100) were connected to the main unit, while a high-performance pH electrode (Metrohm, No. 6.0258.600) and a 5-ring conductivity measuring cell (cell constant: 0.7 cm^{-1}, Metrohm No. 6.0920.100) were attached to the pH and conductivity module, respectively. The pH electrode was calibrated using a three-point procedure with buffer solutions from Metrohm. Calibration of the calcium ion-selective electrode was achieved by titration of a 0.5 M $CaCl_2$ solution into 50 mL deionized water. To induce $Ca(OH)_2$ precipitation, a 0.5 M solution of $CaCl_2$ and a 1 M solution of NaOH were added continuously into a reservoir of deionized water

(initial volume: 50 mL), using two synchronous burettes with a dosing rate per burette set to 0.1 or 0.2 mL/min. During this co-titration procedure, proper mixing in the reservoir was ensured by a magnetic stirrer rotating at short distances to the outlets of the two burettes. To avoid uptake of atmospheric CO_2 and carbonation of the system, all titrations were performed in a closed beaker purged with a continuous flow of water-saturated nitrogen. The same approach was used for experiments in the presence of poly(acrylic acid), which was dissolved at a concentration of 100 ppm in the 50 mL water reservoir prior to addition of $CaCl_2$ and NaOH.

2.3 Small-Angle X-Ray Scattering (SAXS)

Time-resolved in-situ SAXS measurements were carried out at the ID02 beamline of the European Synchrotron Radiation Facility (ESRF, Grenoble, France). Experiments were performed at 12.4 keV and two-dimensional (2D) scattered intensities were collected at small angles with a Pilatus 300K large-area pixel-array detector, with an acquisition time per frame of 0.5 s. Sample transmission was measured using a photodiode installed in the beamstop of the SAXS detector. Solution from the reservoir of the titration assay was continuously pumped (at ca. 100 mL/h) through a Kapton capillary aligned with the X-ray beam. As background and references, an empty Kapton capillary cell (inner diameter: 0.1461 cm), a capillary filled with water, and capillaries filled with $CaCl_2$ and NaOH solutions at different concentrations (covering the full range of concentrations reached in the titration assays) were measured under the same experimental conditions.

The intensity scattered at low angles by a system containing two different populations of particles, including a polydispersity model for the smaller particles, can be approximated by:

$$I_{SAXS} = I_{P1} + I_{P2} = (\Delta\rho_1)^2 N_1 V_1^2 P_1(q) + (\Delta\rho_2)^2 N_1 P_2(q)$$

where $(\Delta\rho_{1,2})^2$ is the so-called contrast (i.e. the (squared) density difference between the particles and the solution), $N_{1,2}$ is the total number of scatterers, $V_{1,2}$ is the volume of the particles and q is the scattering vector. $P_{1,2}(q)$ is the form factor of the particles, which corresponds to the squared Fourier transform of their electronic density distribution.[39] In this model, we do not explicitly consider any structure factor S(q), which would describe the character of interparticle interactions. This does not mean that such interactions do not exist, but the main purpose of the model was to identify different size populations of scatterers, regardless how these scatterers are conceptually interconnected with each other (e.g. aggregates of particles vs. independent populations). For P_1 (i.e. the population of large particles), there was not enough information in the scattering patterns to allow their size and shape (and thus, their volume) to be determined, nor their contrast and concentration. Therefore, only the Porod region was modeled with a power-law form factor, for which a log-normal distribution was used in the model of non-interacting spherical particles:

$$I_{P1}(q) = Aq^n$$

where A accounts for the volume, number and contrast of the particles. The population of small particles (P_2) was analyzed using a polydispersity model based on a log-normal distribution of spherical particles. This model has been shown to give an accurate description of size distributions of grains that are typically obtained from nucleation and growth processes.[40]

$$I_{P2}(q) = (\Delta\rho_2)^2 N_2 \int_0^\infty n(r,R,\sigma)V^2(r)\frac{9(\sin(qr) - qRcos(qr))^2}{(qr)^6}$$

$$\text{Normalization Factor } = \int n(r,R,\sigma)V^2\,dR$$

The probability density function of the log-normal distribution is given by:

$$n(r, R, \sigma) = \frac{1}{\sigma\sqrt{2\pi}r} exp\left(-\frac{[\ln(r) - R]^2}{2\sigma^2}\right)$$

where *R* is the average of the distribution and σ is the standard deviation or shape parameter. The integral over the whole r range was normalized to 1. The total intensity given by this model can therefore be written as follows:

$$I_{SAXS} = Aq^n + (\Delta\rho_2)^2 N_2 \int_0^\infty n(r, R, \sigma) V(r)^2 \frac{9(\sin(qr) - qRcos(qr))^2}{(qr)^6}$$

Modelling of the background-corrected SAXS data was performed using the software IRENA.[41]

2.4 Analytical Ultracentrifugation (AUC)

The size and properties of species present at different stages of the titration assay were explored by AUC sedimentation velocity experiments, which were performed on a Beckman-Coulter XL-I centrifuge using Rayleigh interference optics at 25 °C and 60000 rpm. Aliquots drawn from the titration reservoir were filled into the AUC cell under nitrogen atmosphere. The diffusion coefficient (*D*) of the detected species was determined by using Svedberg equation:[42]

$$D = \frac{sRT}{M(1 - \bar{\nu}\rho_S)}$$

where *s* is the sedimentation coefficient of the detected species, *M* their molecular mass, $\bar{\nu}$ their specific volume, *R* the universal gas constant, *T* the temperature, and ρ_S the density of the solvent. The apparent hydrodynamic diameter of the detected species can then be calculated via the Stokes-Einstein equation:

$$d_H = \frac{k_B T}{3\pi\eta_S D}$$

where k_B is the Boltzmann constant and η_S is the density of the solvent.

2.5 Dynamic light scattering (DLS)

At various stages throughout the titration experiments, samples of the solution were collected under a flow of water-saturated nitrogen and transferred into a cuvette, which was then sealed to prevent carbonation. Dynamic light scattering experiments were performed on a Malvern Zetasizer Nano ZSP using a He/Ne laser (λ = 633 nm) and a scattering angle of 173°. From the measured diffusion coefficients, intensity-weighted distributions of hydrodynamic particle sizes were calculated using the Stokes-Einstein equation.

2.6 Cryo-Transmission Electron Microscopy (cryo-TEM)

Aliquots (4 µL) were collected from the solution reservoir during titration at different times (and thus different nominal levels of supersaturation) using a volumetric pipette and rapidly transferred to lacey carbon grids (200 mesh, Science Services), which were pre-treated by glow discharge for 15 s and subsequently equilibrated at 15 °C and 100 % relative humidity (RH). The solution droplet on the grid was immediately blotted and plunged into liquid ethane using an automated plunge freezer (Vitrobot Mark II, FEI). The resulting vitrified thin films were stored in liquid nitrogen until they were transferred to a cryo-TEM sample holder (CT3500, Gatan). Specimens were imaged at -180 °C using a Tecnai G2 F20ST microscope from FEI at an acceleration voltage of 200 kV in low-dose mode, in order to avoid beam damage.

2.7 Pair Distribution Function (PDF) Analyses

In-situ and time-resolved high-energy X-ray scattering (HEXS) measurements were carried out at beamline ID15a of the European Synchrotron Radiation Facility (ESRF, Grenoble, France). Experiments were performed using an X-ray beam (size: 200 µm x 200 µm) at 63 keV, which was aligned with a Kapton capillary (inner diameter: 0.1461 cm) connected to a flow-through setup. Scattered intensities were collected in the form of 2D diffraction patterns with a DECTRIS Pilatus3 X CdTe 2M detector. During co-titration of 0.5 M $CaCl_2$ and 1 M NaOH into 50 mL

deionized water at a dosing rate of 0.1 mL/min each, the solution in the reaction vessel was circulated through the Kapton capillary using a peristaltic pump (Gilson MiniPuls 3) at a flow rate of ca. 10 mL/s, while scattering patterns were recorded continuously with an exposure time of 10 s. Background patterns were collected for an empty Kapton capillary, as well as capillaries filled with deionized water and 34 mM NaCl in water. From the recorded 2D scattering data, atomic pair distribution functions (PDFs) were obtained by using the PDFgetX3 software package.[43]

2.8 Ex-Situ Characterization

The (solid) phases formed during the precipitation reaction were isolated from solution by rapid filtration under inert gas atmosphere, washed by small amounts of water and ethanol, and subsequently dried and stored in a desiccator under nitrogen atmosphere to avoid carbonation. For scanning electron microscopy (SEM), the dried powders were fixed on sample holder by double-sided adhesive tape and covered with a 6 nm thick layer of platinum using a Quorum Q150R sputter-coating instrument. SEM images were acquired on a Zeiss Auriga 40 field-emission microscope at an acceleration voltage of 5 kV. Thermogravimetric analyses (TGA) were performed on a Netzsch STA 449F3 instrument. A sample mass of 10 mg was heated from 30 to 1000 °C at a rate of 10 K/min under a flow of nitrogen at 10 L/min. Powder X-ray diffraction (PXRD) patterns were recorded over a 2θ range of 5-80° using a Bruker AXS D8 Advance diffractometer, operated in Bragg-Brentano configuration and equipped with a IμS-X-ray source providing Cu-K_α radiation (λ = 1.542 Å) and a Lynxeye XE detector. The mechanical properties of the formed portlandite precipitates were characterized by means of nanoindentation experiments using an Agilent G200 system. Samples were prepared by gluing on a glass slide and were subsequently indented by a well-defined diamond tip with Berkovich geometry, while

monitoring the applied load and indentation depth of the tip. The load function was set to a load/unload rate of 67 μN/s and a maximum load of 0.5 mN, with a hold segment of 30 s. From the obtained load-displacement curves, the local reduced E-modulus was determined. Finally, in the experiments with added poly(acrylic acid), the initial polymer solution (100 ppm) as well as the supernatant liquid after portlandite precipitation via co-titration were analyzed with respect to their total organic carbon (TOC) content, using a Shimadzu TOC-L instrument. The samples were centrifuged to remove solid matter and passed through syringe filters (450 nm) prior to analysis.

3. Results and Discussion

3.1 Nucleation of Portlandite in the Absence of Additives

In order to study the nucleation pathway of portlandite from aqueous solution, we developed a co-titration assay, in which 0.5 M $CaCl_2$ and 1 M NaOH stock solutions are added at equal rates (0.1 or 0.2 mL/min) into a reservoir of water with an initial volume of 50 mL. In this way, the saturation with respect to portlandite is gradually increased while maintaining an equimolar calcium:hydroxide ion ratio (in contrast to titrations performed by Rodriguez-Navarro et al. in their recent study,[36] where $CaCl_2$ was added to an excess of NaOH, resulting in a continuous variation of ion stoichiometry). During co-titration, the concentration of free Ca^{2+} ions as well as turbidity, conductivity and pH (as a direct measure for the free hydroxide concentration) in the reservoir were continuously monitored by several immersed probes. Typical time-dependent profiles obtained from such co-titration experiments are shown in Figure 1. In terms of $c_{free}(Ca^{2+})$, the procedure results in classical LaMer-type diagrams,[44] where the amount of free Ca^{2+} ions increases until a maximum is reached (at $c_{added}(Ca^{2+})$ = 47.6 mM and $c_{free}(Ca^{2+})$ = 25.5 mM), after which the free calcium concentration drops rapidly, signifying nucleation (Figure 1a).

In the following, $c_{free}(Ca^{2+})$ continues decreasing towards a constant plateau (indicated by the dashed horizontal line in Figure 1a), which corresponds to the solubility of the formed phase. Essentially, the same qualitative behavior is also observed for the evolution of the free OH^- concentration during co-titration (Figure 1b), confirming the interaction of the two ions and their common precipitation. From the ion concentrations at the plateau after nucleation and early growth, the solubility product of the precipitated phase can be determined as $c_{free}(Ca^{2+}) \cdot c_{free}(OH^-)^2 = 2.2 \cdot 10^{-5}\ M^3$, which is considerably higher than values reported for crystalline portlandite in the literature ($5.02 \cdot 10^{-6}\ M^3$).[33] These differences could indicate the (co-)existence of a more soluble phase (e.g. ACH) after nucleation, but might also be related to the absence of carbon dioxide in the present solutions, which should result in a higher pH compared to a system in contact with CO_2 (as in the case of the mentioned previous work). The latter notion is confirmed by a comparison of pH values calculated based on the reported K_{sp} (12.3) and measured in our study (12.5). Higher pH corresponds to higher free hydroxide concentrations and hence, the determined solubility product of portlandite appears higher as well. Before reaching their maximum, the detected concentrations of free Ca^{2+} and OH^- ions were consistently lower than the dosed amounts (solid black lines in Figure 1a and 1b). This suggests the formation of ion pairs/complexes and, potentially, larger clusters in the pre-nucleation regime, as reported for $CaCO_3$ in earlier studies[5,46] and proposed for portlandite in a recent work.[36]

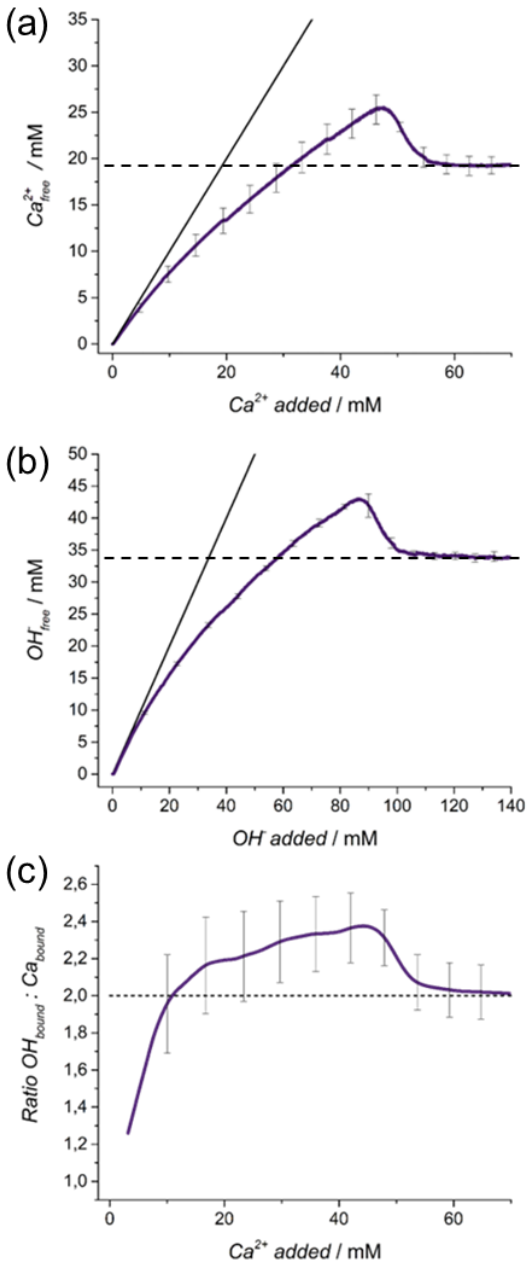

Figure 1. In-situ monitoring of solution speciation during portlandite precipitation from solution via co-titration of 0.5 M $CaCl_2$ and 1 M NaOH into water (initial volume: 50 mL) at a dosing rate of 0.2 mL/min each. (a) Time-dependent evolution of the concentration of free calcium ions in solution, as measured by an ion-selective electrode (purple line, average of three independent experiments, with error bars representing ± 1-σ standard deviation) and compared to the respective dosed amount (black line). (b) Time-dependent evolution of the concentration of free hydroxide ions in solution, as measured by a pH electrode (purple line, average of three independent experiments, with error bars representing ± 1-σ standard deviation) and compared to the respective dosed amount (black line). (c) Molar ratio of bound calcium to bound hydroxide ions during co-titration, given as averaged values (with ±1-σ standard deviation) obtained from three independent titration experiments.

Interestingly, the ratio of bound ions was not constant during the titration experiment, as shown in Figure 1c: in the early (undersaturated) stages of the pre-nucleation regime, the OH^-:Ca^{2+} ratio was found to be in the range of 1.2:1 to 1.3:1, indicating the formation of – on average – positively charged ion complexes (i.e. $[Ca(OH)_x]^{y+}$, with y = 2-x). Upon addition of growing amounts of calcium and hydroxide ions, the ratio of bound ions increases until it reaches a value of ca. 2:1, corresponding to neutral complexes (i.e. $[Ca(OH)_2]^0$), at about 10 mM added Ca^{2+}, which coincides with the solubility limit and thus the transition from the under- to the supersaturated regime. Towards critical levels of supersaturation, the OH^-:Ca^{2+} ratio increases further up to almost 2.4:1 shortly before the onset of nucleation (i.e. the drop in free calcium and hydroxide concentration), suggesting the presence of at least a certain fraction of negatively charged complexes (i.e. $[Ca(OH)_{(2+z)}]^{z-}$) in this regime at the given high pH (ca. 12.5 near the maximum in $c_{free}(OH^-)$). Upon nucleation and early growth, the ratio of bound ions decreases and, along with the ion product approaching the solubility plateau, converges towards a value of 2:1, as expected for solid portlandite.

All considerations made so far tacitly relied on the assumption that the aqueous electrolyte solutions of interest can be treated as ideal systems with negligible influence of activity coefficients. In fact, the ionic strength increases from zero (at the beginning) up to ca. 138 mM (assuming no ion pairing/clustering) or at least 72 mM (assuming the solutions to be ideal and all calcium as well as hydroxide ions to bind in neutral complexes/clusters) at the maximum during co-titration. In either of these two extreme cases, the nominal ionic strength clearly exceeds regimes where ideal behavior should be sustained. However, given that ideal treatment of the co-titration data eventually yields consistent compositions for bulk portlandite (i.e. Ca^{2+}:OH^- ≈ 2:1, cf. Figure 1c), we consider the observed ion binding stoichiometries in the early and later pre-

nucleation stages to be real. Based thereon, ion association in the pre-nucleation regime can be further analyzed on a microscopic level within the framework of a so-called multiple-binding equilibrium, which can be formulated for calcium and hydroxide "binding centers" as follows (in full analogy to pre-nucleation equilibria in the $CaCO_3$ system):[47]

$$\mathrm{OH^-} \underset{-Ca^{2+}}{\overset{+Ca^{2+}}{\rightleftharpoons}} (\mathrm{OHCa})^+ \underset{-Ca^{2+}}{\overset{+Ca^{2+}}{\rightleftharpoons}} (\mathrm{OH(Ca)_2})^{3+} \underset{-Ca^{2+}}{\overset{+Ca^{2+}}{\rightleftharpoons}} \ldots$$

$$\mathrm{Ca^{2+}} \underset{-OH^-}{\overset{+OH^-}{\rightleftharpoons}} (\mathrm{CaOH})^+ \underset{-OH^-}{\overset{+OH^-}{\rightleftharpoons}} (\mathrm{Ca(OH)_2})^{(0)} \underset{-OH^-}{\overset{+OH^-}{\rightleftharpoons}} \ldots$$

Binding of calcium ions to a central hydroxide ion can be quantified using the co-titration data and the following simplified equation:[47]

$$\nu(\mathrm{Ca^{2+}}) = \frac{n_{\mathrm{added}}(\mathrm{OH^-})}{n_{\mathrm{bound}}(\mathrm{Ca^{2+}})} = \frac{1}{x(\mathrm{Ca^{2+}})} + \frac{1}{x(\mathrm{Ca^{2+}}) \cdot K(\mathrm{Ca^{2+}})} \cdot \frac{1}{c_{\mathrm{free}}(\mathrm{Ca^{2+}})}$$

where $x(Ca^{2+})$ is the number of calcium ions binding to a hydroxide ion on a microscopic level and $K(Ca^{2+})$ the microscopic equilibrium constant of this process. An analogous equation can also be formulated for the *vice versa* scenario of multiple OH^- ions binding to a central Ca^{2+} ion:

$$\nu(\mathrm{OH^-}) = \frac{n_{\mathrm{added}}(\mathrm{Ca^{2+}})}{n_{\mathrm{bound}}(\mathrm{OH^-})} = \frac{1}{x(\mathrm{OH^-})} + \frac{1}{x(\mathrm{OH^-}) \cdot K(\mathrm{OH^-})} \cdot \frac{1}{c_{\mathrm{free}}(\mathrm{OH^-})}$$

Added, free and bound amounts of hydroxide and calcium ions have been determined experimentally by potentiometry as described above (cf. Figure 1), allowing for a calculation of $\nu(Ca^{2+})$ and $\nu(OH^-)$ at each point of the titration experiment. Plots of the two parameters as functions of $1/c_{free}(Ca^{2+})$ and $1/c_{free}(OH^-)$, respectively, are shown in Figure 2 for added

concentrations of 3-30 mM Ca^{2+} and 6-60 mM OH^-, i.e. up to the point where nominal saturation with respect to portlandite is reached.

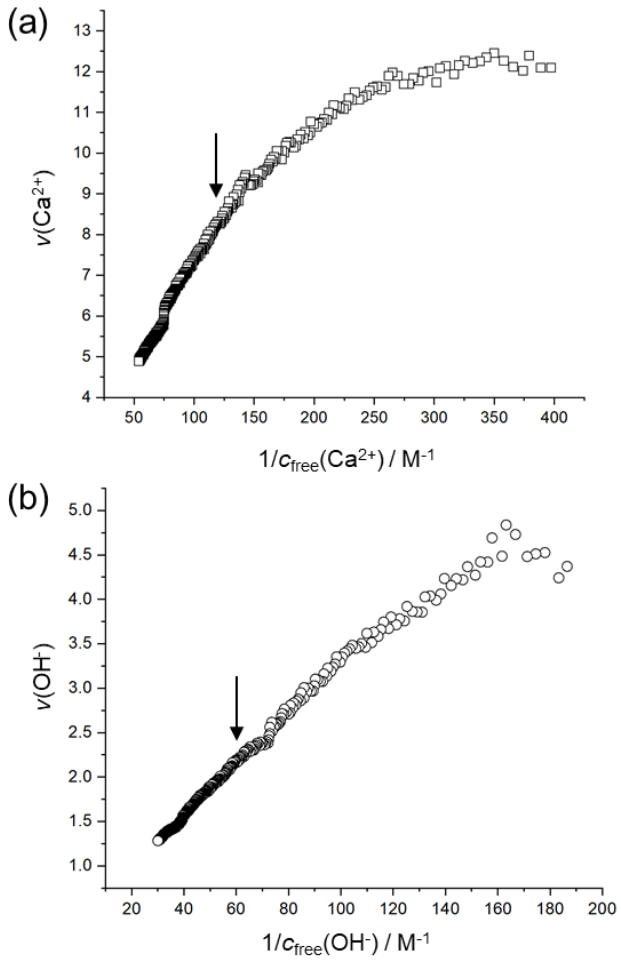

Figure 2. Analysis of ion association in the pre-nucleation regime according to the model of a multiple-binding equilibrium,[46] where (a) hydroxide and (b) calcium is considered as the central ion. Arrows indicate the point at which the macroscopic ratio of bound hydroxide to bound calcium changes from <2:1 to >2:1 during co-titration (cf. Figure 1c).

In both cases, non-linear behavior is observed at low ion concentrations (i.e. at large values of $1/c_{free}$, especially for $\nu(Ca^{2+})$), which indicates a progressive change in ion association as the level of saturation is gradually increased. Linear fits of different intervals of the two plots show

that both microscopic numbers of binding sites increase during titration (with $x(OH^-)$ being generally higher than $x(Ca^{2+})$) and adopt a more or less constant value once the macroscopic ratio of bound hydroxide to bound calcium reaches 2:1 (indicated by the black arrows in Figure 2). Fits above this threshold (i.e. for 10 mM $\leq c_{added}(Ca^{2+}) \leq$ 30 mM) yield $x(OH^-) = 2.34$ and $x(Ca^{2+}) = 0.46$, suggesting that there are significantly more binding sites for OH^- on Ca^{2+} than *vice versa*. The macroscopic equilibrium constant of ion association can be obtained *via* $K = x(Ca^{2+})\cdot K(Ca^{2+}) = x(OH^-)\cdot K(OH^-)$ and was found to be about 20-40 M^{-1}. It is important to note that $x(Ca^{2+})$ and $x(OH^-)$ are average values over all states of association – including the respective free ions (for which the binding sites are not occupied).[46] To access the coordination in bound states only (N), both parameters thus need to be related to the bound fraction of the respective ion (i.e. $f_{bound}(Ca^{2+})$ and $f_{bound}(OH^-)$), which can readily be deduced from the actual amounts of added and free ions measured in the titration experiments (cf. Figure 1; with $f_{bound} = 1 - c_{free}/c_{added}$). Using $N = x / f_{bound}$, one obtains $N(Ca^{2+}) \approx 1.4$ and $N(OH^-) \approx 5.8$, which shows that calcium ions are coordinated by almost six hydroxide ions in bound states on average. In addition, the fact that $N(Ca^{2+})$ is higher than unity implies that the bound species cannot be solely mononuclear complexes (like $Ca(OH)_6^{4-}$, for which $N(Ca^{2+}) = 1$), but must also include bi- or polynuclear entities where hydroxide ions presumably act as bridges between different calcium centers (i.e. Ca-OH-Ca units, for which $N(Ca^{2+}) = 2$). In other words, the investigated electrolyte solutions appear to contain both mononuclear complexes and larger PNCs already before the system becomes supersaturated with respect to portlandite – in analogy with other minerals such as calcium carbonate.[5,46]

To characterize the species formed along the nucleation pathway of portlandite, we performed in-situ SAXS measurements on the system at different stages of the precipitation process, as

summarized in Figure 3. A sequence of time-resolved scattering patterns recorded during the simultaneous titration of 0.5 M $CaCl_2$ and 1 M NaOH into 50 mL deionized water at a dosing rate of 0.2 mL/min each is shown in Figure 3a. First signs of significant scattering from crystallization precursors in the bulk ensemble were observed in SAXS patterns collected after 41.7 mM $CaCl_2$ had been added, i.e. in the supersaturated regime prior to the maxima in $c_{free}(Ca^{2+})$ and $c_{free}(OH^-)$. From this point onwards, two distinct populations (P) of scattering species can be differentiated in the SAXS data, as visualized for added Ca^{2+} concentrations of 43.0 and 48.4 mM in Figure 3b and 3c, respectively: a population P_1, described by the pink component, with apparent diameters in the range of 3-4 nm, and another population P_2, described by the orange component, with significantly larger diameters of >100 nm. The size of the population of smaller species (P_1) increases only slightly over time (from (3.2 ± 0.4) at 43.0 mM added Ca^{2+} to (4.0 ± 0.3) nm at 48.4 mM), while their number density remains approximately constant, within the limits of experimental accuracy, throughout the entire duration of the co-titration assay. In terms of size, the species of population P_1 resemble pre-nucleation clusters and primary particles reported to be earliest precursors to the solution-mediated crystallization of calcium carbonate[47] and calcium sulfate,[13,48] respectively.

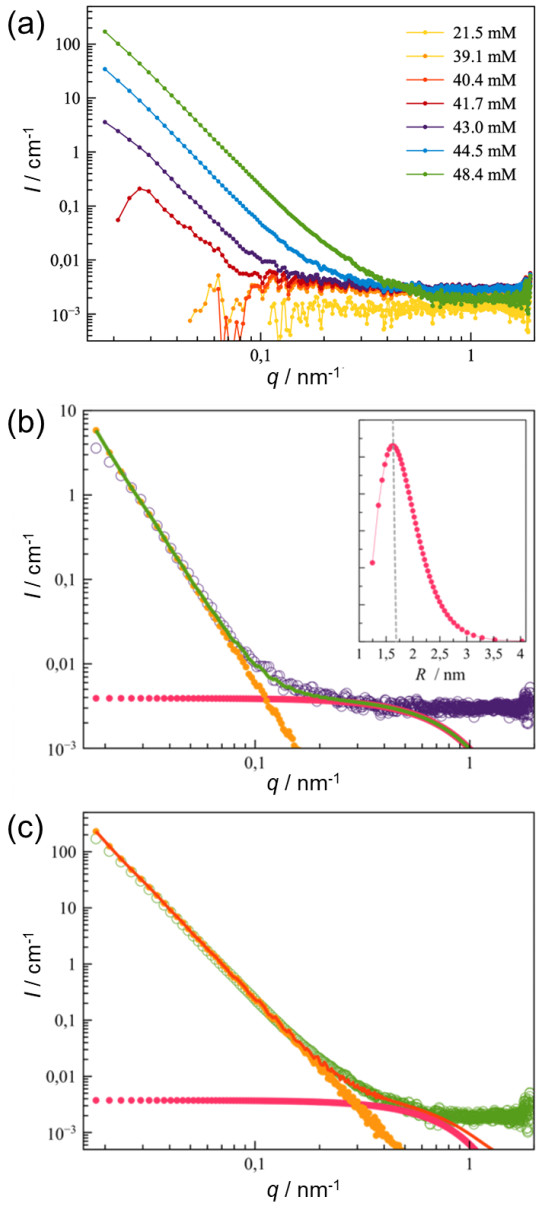

Figure 3. Results of in-situ SAXS measurements during the formation of portlandite from solution. (a) SAXS patterns acquired at different times (here given as the equivalent concentrations of added Ca^{2+} ions) during co-titration of 0.5 M $CaCl_2$ and 1 M NaOH into 50 mL water at individual dosing rates of 0.2 mL/min. (b) Experimental SAXS pattern (purple circles) obtained after 3780 s (corresponding to 43.0 mM of added Ca^{2+}). The data was fitted (green line) using two particle populations P_1 (pink dots) and P_2 (orange dots), respectively representing small species that dominate scattering at high q with an average diameter (3.2 ± 0.4) nm, and larger species (> 00 nm) that dominate scattering in the low- and intermediate-q range. In the regime of high angles (q > 1 nm^{-1}), scattering is dominated by the ionic background, which was not explicitly fitted here. The inset shows the resulting log-normal size distribution of the small population. (c) Experimental SAXS pattern (green circles) obtained after 4302 s (corresponding to 48.4 mM of added Ca^{2+}). Again, the integral signal can be fitted (red line) by assuming

two populations (same color code as in (b)), whereby the average size of the smaller species has increased to (4.0 ± 0.3) nm.

With proceeding addition of calcium and hydroxide ions, the SAXS intensity contributed by the larger species (P_2) increases (cf. Figure 3a). This can be due to an increase of their number density or their size, or both. The exact reason cannot be discerned due to the limited accessible q range, with a minimum at 0.02 nm^{-1}. Based on these observations, we assume that the smaller population traced by SAXS consists mainly of calcium hydroxide clusters (with varying stoichiometries), whereas the larger population comprises nanoparticles and/or -droplets, which may have formed through aggregation of the smaller species.

Another powerful technique to explore the nature of the early pre-nucleation species in solution is analytical ultracentrifugation. Exemplarily, the size distribution of species detected in a sample drawn after addition of 35 mM $CaCl_2$ is shown in Figure 4. Due to the applied high centrifugal force, AUC only detects the smaller species present in solution at this stage, whose average diameter was found to be ca. 2.2 nm – in reasonable agreement with the SAXS results (note that samples investigated by SAXS were drawn at later times, where the clusters in solution had likely already grown to slightly larger sizes).

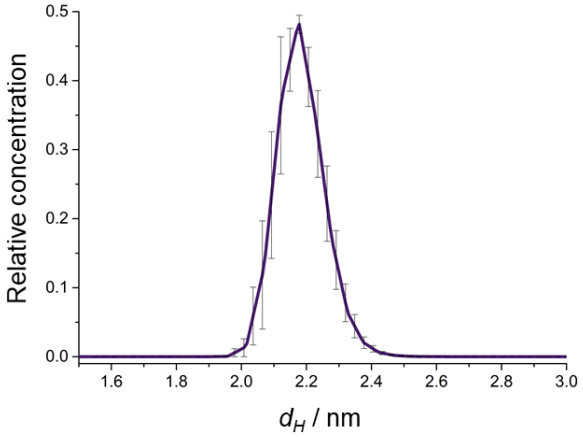

Figure 4. Size distribution obtained from AUC analyses of a sample drawn from the co-titration experiment (0.5 M $CaCl_2$ and 1 M NaOH into 50 mL water at 0.2 mL/min) after addition of 35 mM $CaCl_2$.

Using the average hydrodynamic diameter (d_H) and the simultaneously determined sedimentation coefficient (s), the density of the detected calcium hydroxide clusters ($\rho_{Clusters}$) can be estimated using the following equation:[42]

$$\rho_{\text{Clusters}} = \frac{18\eta_0 s}{d_H^2} + \rho_0$$

where η_0 and ρ_0 are the viscosity and density of water. Such calculations give cluster densities in the range of 1.0-1.1 g/mL, i.e. values that are close to pure water and much lower than expected for (crystalline) portlandite (ca. 2.2 g/mL).[49] This suggests that the detected calcium hydroxide clusters are heavily hydrated and can be viewed as liquid-like species rather than solid particles, much like what has been reported for the earliest precursors of $CaCO_3$ crystallization.[4]

To gain further insights into the species and precursor phases relevant for portlandite formation from solution, aliquots were drawn from the titration vessel at different times (ranging from the undersaturated regime up to the maximum in $c_{free}(Ca^{2+})$), quenched through rapid vitrification and imaged using cryo-TEM (Figure 5). Already after addition of ~28 mM Ca^{2+}, i.e., at a stage where the system is still undersaturated with respect to the finally formed phase (cf. Figure 1a), rounded particles with diameters in the range of 150-200 nm were observed, which did not produce any diffraction spots or rings in selected-area electron diffraction (SAED) patterns (Figure 5a). These particles may thus be considered as amorphous calcium hydroxide (ACH), as already found by Rodriguez-Navarro et al. based on room-temperature TEM studies.[36] The fact that such ACH structures were already observed in cryo-TEM at a stage where SAXS did not

detect any significant bulk scattering indicates that only few amorphous nanoparticles exist at this point.

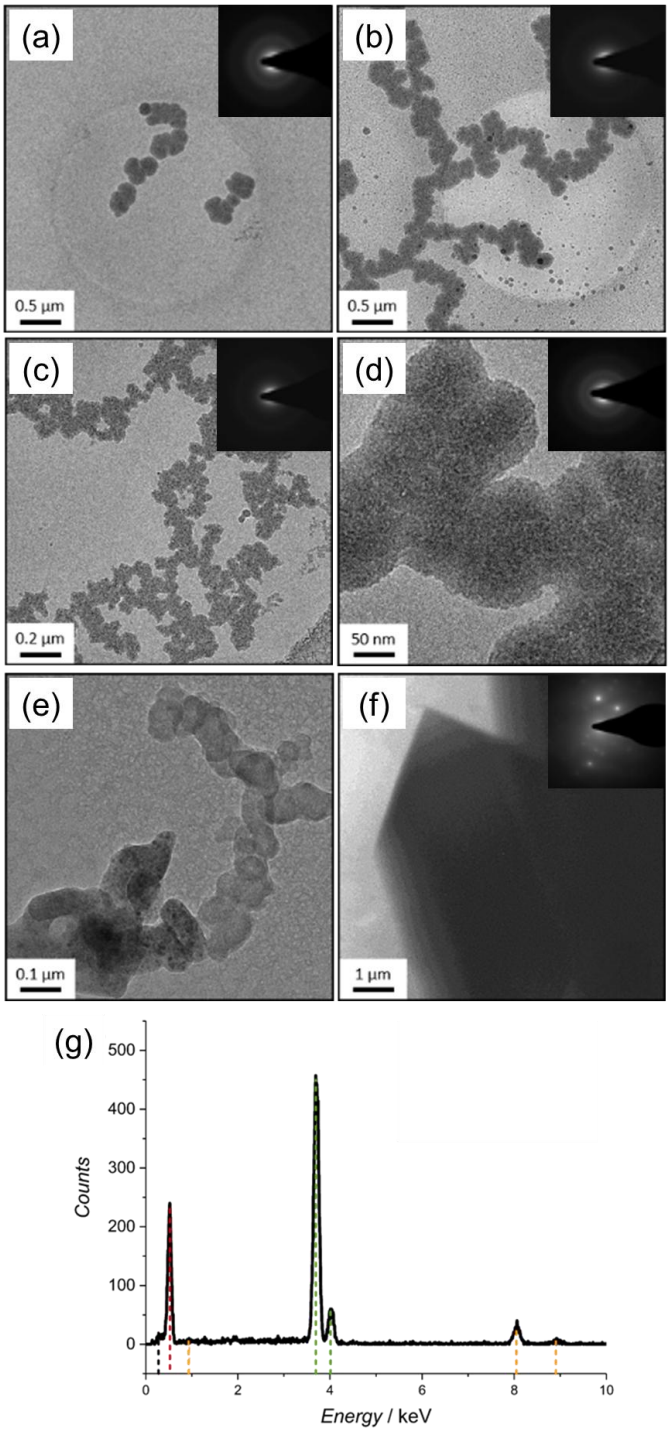

Figure 5. Cryo-TEM images of samples drawn from the co-titration experiment (0.5 M $CaCl_2$ and 1 M NaOH into 50 mL water at 0.2 mL/min) after addition of (a) 28, (b) 34, (c) 38, (d) 42, (e) 46 and (f) 49

mM $CaCl_2$. Insets: SAED patterns acquired from the respective shown field of view. (g) EDX spectrum collected from the crystals shown in (f), with strong signals from calcium (green) and oxygen (red), weaker signals from copper (orange) and traces of carbon (black) (both originating from the used carbon-filmed copper grids).

Furthermore, the absence of any noticeable discontinuity in the titration profiles means that the ACH particles form from a population of already bound ions, which are no longer in (fast) equilibrium with the free ions and/or that the presumed particles are actually dense liquid phases (or particles embedded in such liquid phases) without a defined solubility product – again in analogy to the $CaCO_3$ system.[5,50] In other words, cluster aggregation and coalescence into dense liquid phases and/or ACH nanoparticles appear to determine the rate of the process and pose the actual barrier to nucleation, such that only few particles can form at this stage and the concentrations of free calcium and hydroxide ions are not yet significantly affected by the incipient process of nanoscopic phase separation. Upon further addition of ions, the ACH nanoparticles aggregate and form chain-like structures (Figure 5b) as the system enters the supersaturated regime. At still higher Ca^{2+} and OH^- concentrations, these aggregates become more pronounced and develop into spacious networks (Figure 5c), which continue to grow and densify. Close-up views of individual particles in such networks (Figure 5d) reveal a granular texture, which may be interpreted as evidence for the ACH phase being constituted of the nanoclusters detected by both SAXS and AUC analyses. The amorphous phase persists up to the maximum in $c_{free}(Ca^{2+})$ (Figure 5e), but subsequently transforms into crystalline particles, as evidenced by diffraction spots in SAED patterns (Figure 5f). The observed crystals measure several micrometers in size, display well-developed facets, and were confirmed to be calcium hydroxide by energy-dispersive X-ray (EDX) analysis (Figure 5g).

The existence and nature of an intermediate ACH phase was further explored by means of in-situ high-energy X-ray scattering (HEXS) measurements and subsequent pair distribution function (PDF) analysis (Figure 6).

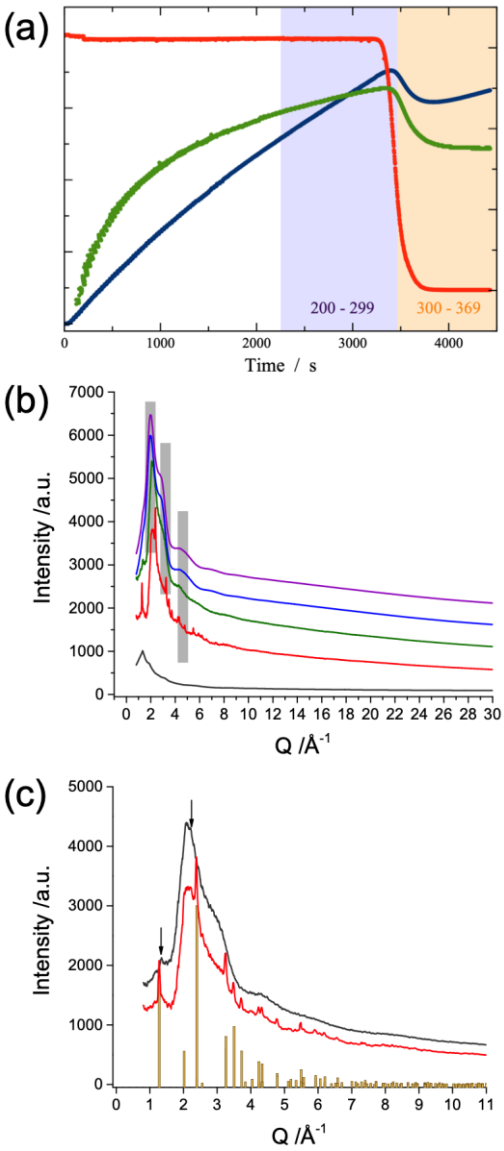

Figure 6. In-situ monitoring of portlandite formation using potentiometric co-titration and high-energy X-ray scattering. (a) Time-dependent evolution of the calcium potential (green), conductivity (blue) and transmittance (orange) simultaneous addition of 1 M NaOH and 0.5 M $CaCl_2$ into 50 mL deionized water at a dosing rate of 0.1 mL/min each. (b) Background-subtracted diffraction patterns obtained by averaging frames 200-299 (green) and 300-369 (red), respectively indicated by the purple- and orange-shaded areas in (a). For comparison, diffraction patterns obtained for bulk water (blue), an empty Kapton capillary

(black), and bulk water after correction for scattering from the Kapton capillary (purple) are also shown. The intensities of these three background patterns were scaled down by a factor of 30 for better comparability with the water-subtracted 200-299 and 300-369 patterns. An offset of 500 a.u. between the patterns was introduced for the sake of clarity. (c) Background-corrected diffraction patterns obtained by averaging frames 200-299 (blue) and 300-369 (red) in the low-*q* region, as compared to a reference diffraction pattern of crystalline portlandite (vertical lines) reported in the literature.[51]

In total, 369 diffraction patterns were collected during the slow (0.1 mL/min) co-titration of 1 M NaOH and 0.5 M $CaCl_2$ into 50 mL deionized water, while continuously monitoring the Ca^{2+} potential, conductivity and transmittance of the solution in the reaction vessel (Figure 6a). During the early stages of the titration process, mineral precursors were present only at very low volume fractions and thus, individual diffraction patterns did not contain any obvious signal other from pure water, even after subtraction of scattering from the bulk solvent. In order to increase the signal-to-water background ratio, the collected data were averaged into groups of 100 frames (0-99, 100-199, 200-299) before the drop in calcium potential, conductivity and transmittance, and all acquired frames after the drop (300-369) were also averaged. After bulk water background subtraction, the clusters of 200-299 and 300-369 frames showed diffraction patterns of two distinct solid phases (Figure 6b): reflections observed after averaging data during the later stages (frames 300-369) match reference diffractograms of portlandite (Figure 6c) found in the literature.[51] However, the averaged diffraction pattern obtained from the earlier stages (200-299) contains far less pronounced peaks (indicated by arrows in Figure 6c), which are also slightly shifted with respect to the corresponding reflections of crystalline portlandite. It is worth noting that despite background subtraction, the HEXS patterns of both detected solid phases still contain major contributions from scattering of water (namely the three broad correlation "bumps" highlighted by gray strips in Figure 6b). Attempts to completely subtract the water background resulted in negative intensity values in the low-*q* part of the data. This suggests that the observed contribution originates from an aqueous component, which is linked to the

diffracting phases and their partially amorphous and/or hydrated character (e.g. the ion clusters detected by both SAXS and AUC). Furthermore, this aqueous component could be to some degree structurally different from any of the bulk counterparts, for example a mixture of a solid amorphous phase and water, i.e., non-bulk water.

Conversion of the HEXS diffractograms into real-space pair distribution functions, $G(r)$, provides further insight into the local structure and the character of the occurring solid phases (Figure 7). As expected, the $G(r)$ function of water (purple line in Figure 7a) displays relatively broad maxima not extending beyond $r > 10$ Å, which confirms the lack of long-range ordering. The strongest peak at ~2.8 Å represents the typical O-O distance in bulk water.[52] In this region, the pair distribution functions obtained for frame clusters 200-299 and 300-369 (green and red lines in Figure 7a, respectively) are quite similar to water, although the main peak is shifted to slightly lower values (~2.6 Å), as a direct manifestation of the aqueous/amorphous component observed in Figure 6b. This shift might be related to the presence of ions and/or nanoparticles, which can modify the local structure of water.[53,54] In the case of the frame cluster 300-369, one can further see continuous oscillations in $G(r)$ at $r > 10$ Å, which indicate long-range order and thus confirm the (partially) crystalline character of the system at this stage. Such obvious oscillations are absent in the PDF function of the frame cluster 200-299. Subtraction of the scaled $G(r)$ profile of pure water from those of the frame clusters 200-299 and 300-369 yields differential functions, i.e., $dG(r)$, in which long-distance correlations become more apparent (Figure 7b). Although the $dG(r)$ function obtained for the frame cluster 200-299 shows similar features as compared to frame cluster 300-369, there are still significant differences in peak positions (in line with the diffraction patterns in Figure 6c) and the overall quality of the data collected during the earlier stages is rather poor, likely due to the low volume fraction of ordered

scattering species and the dominance of aqueous/amorphous contributions at this point. As portlandite nucleation proceeds, the volume fraction of ordered species increases and thus the differential pair distribution function becomes more distinct over the entire considered range of *r* values.

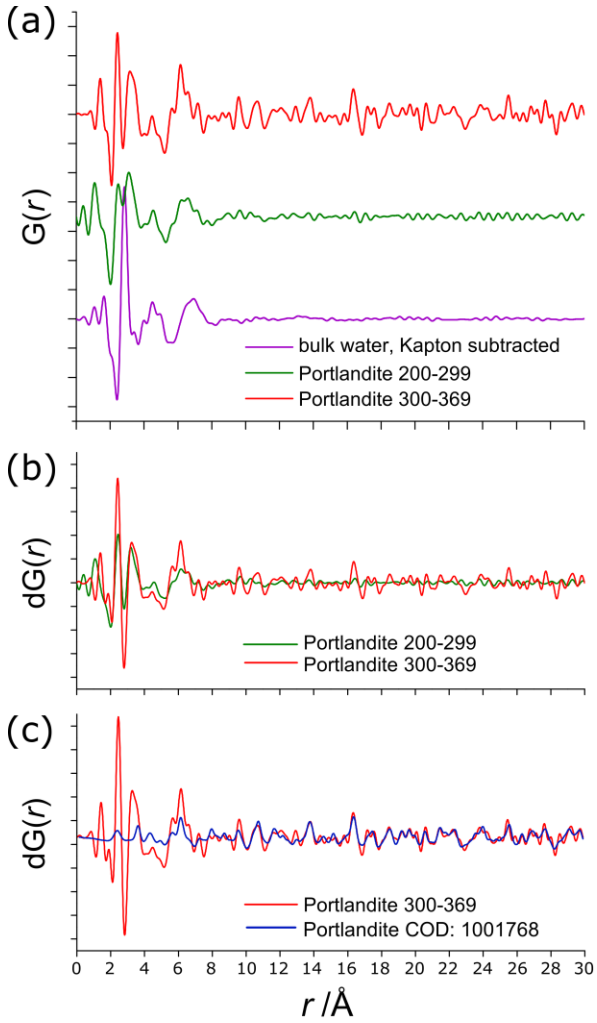

Figure 7. Real-space pair distribution functions, $G(r)$, obtained by Fourier transformation of the experimental high-energy diffractograms shown in Figure 6. (a) Comparison of $G(r)$ profiles obtained for pure water (purple, after subtraction of scattering from an empty Kapton capillary) and the averaged frame clusters 200-299 (green) and 300-369 (red), using q_{max} limits of 13.0 $Å^{-1}$ (pure water and frame cluster 200-299) and 15.2 $Å^{-1}$ (frame cluster 300-369). Note that the high-frequency ripples in the profile

of pure water (and partly also the frame cluster 200-299) are considered to be an artifact of the Fourier transformation, which can be "dampened" by further reduction of q_{max}, with no significant changes in peak positions. (b) Differential pair distribution functions, d$G(r)$, obtained by referencing frame clusters 200-299 (green) and 300-369 (red) to pure water. (c) d$G(r)$ functions obtained by referencing the frame cluster 300-369 (red) and a $G(r)$ dataset of crystalline portlandite from the literature[51] (blue, COD 1001768) to pure water.

In a further comparison, we have calculated differential d$G(r)$ functions by subtracting the profile of pure water from those of the frame cluster 300-369 and crystalline portlandite reported in the literature[51] (Figure 7c). The resulting differential profiles match relatively well, especially in the high-r regime. However, the d$G(r)$ function of frame cluster 300-369 displays peaks at ca. 2.4 and 6.1 Å that are significantly stronger in amplitude than expected for a fully crystalline portlandite phase. The peak at ~2.4 Å matches well the distance between a central calcium ion and oxygen in the first coordination shell, while the broad correlation at ~6.1 Å can be tentatively attributed to interatomic distances to higher-order water coordination shells around the amorphous particles, as reported before for other nanoparticle systems[55] and ion pairs.[56] This suggests that the pair distribution function observed experimentally for frame cluster 300-369 is actually a combination of an already crystalline phase (which dominates the high-r part) and an amorphous (nano)precipitate, whose ordering does not extend beyond ~1 nm. Following the same logic, the measured PDF of the frame cluster 200-299 can be interpreted as a combination of contributions from a predominant disordered phase and a minor amount of a crystalline component. In essence, our HEXS measurements and PDF analyses provide clear in-situ evidence for the occurrence of an amorphous precursor phase during portlandite nucleation from solution, as inferred from ex-situ ambient-temperature TEM investigations in a recent work[36] and cryo-TEM data produced in the present study (cf. Figure 5).

Finally, precipitates formed at the end of the co-titration experiment were isolated and characterized ex situ using scanning electron microscopy and powder X-ray diffraction (Figure 8). SEM images show uniform hexagonal crystals with prism-shaped morphologies, typical diameters of 2-10 µm and lengths in the range of 10-50 µm (Figure 8a-b), as expected for well-developed crystalline portlandite.[57] The formation of virtually phase-pure portlandite and the absence of any crystalline carbonate phases is confirmed by the PXRD patterns (Figure 8c).

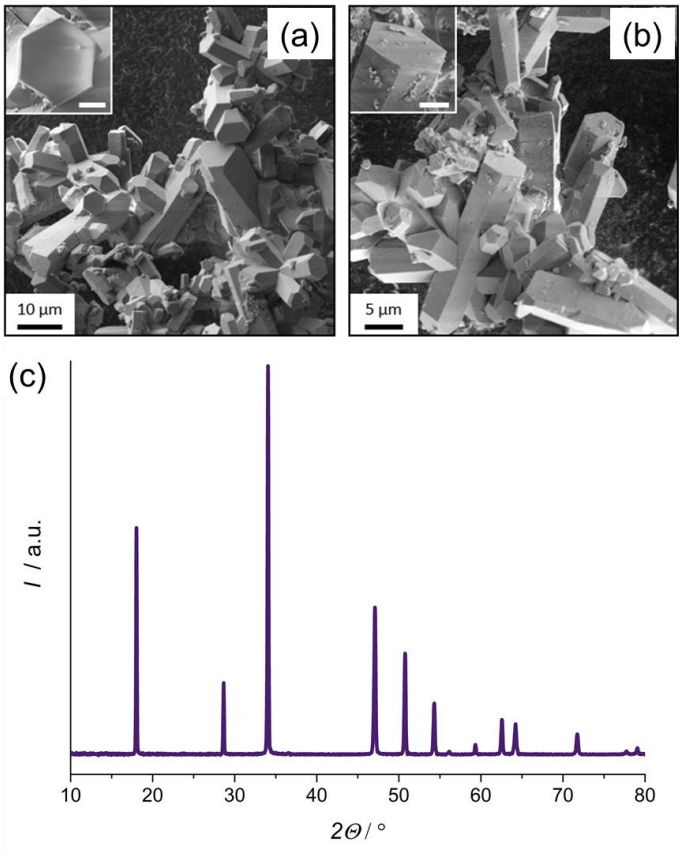

Figure 8. Ex-situ characterization of precipitates formed at the end of the $Ca(OH)_2$ co-titration experiment. (a-b) SEM images showing well-defined hexagonal portlandite crystals (scale bars in insets: 2 µm). (c) XRD pattern of the isolated powders, wherein all observed reflections can be assigned to crystalline portlandite (ICDD 04-0733).[58,59] Note that the absence of the most intense reflection of calcite at 29.7° confirms the formation of a product free of crystalline calcium carbonate.

3.2 Effects of Poly(Acrylic Acid) on the Nucleation of Portlandite from Solution

In order to study the influence of poly(acrylic acid) – as a model polymeric additive commonly used for crystallization control[60-62] – on the early stages of portlandite formation, we have performed co-titrations of 0.5 M $CaCl_2$ and 1 M NaOH (according to the procedure depicted in Figure 1) into a solution of PAA in water (initial concentration: 100 ppm). Exemplary results of such an additive-containing experiment are shown in Figures 9 and 10. In the presence of PAA, the drop in the detected amounts of free calcium (Figure 9a) and hydroxide (Figure 9b) ions, as well as of the net conductivity of the solution (Figure 9c), is shifted towards much higher added concentrations ($c_{added}(Ca^{2+})$ = (75.8 ± 1.4) mM as compared to (47.6 ± 1.8) mM in the additive-free experiment, corresponding to a retardation factor, i.e. a relative delay, of about 1.6). This means that added PAA inhibits the formation of solid calcium hydroxide, which occurs once the maximum in $c_{free}(Ca^{2+})$ and $c_{free}(OH^-)$ is reached (cf. Figures 5-7). Interestingly, the simultaneously monitored turbidity of the solution indicates the presence of relatively large species already after addition of ca. 5 mM Ca^{2+}, as reflected in a pronounced decrease of solution transmission up to $c_{added}(Ca^{2+}) \approx 20$ mM (Figure 10a, red curve). The onset of measurable turbidity in the system coincides with a kink in the calcium potential (cf. Figure 9a), which indicates that the interactions causing the decrease in solution transmission involve Ca^{2+} ions and, arguably, (poly)acrylic acid. In the further course of co-titration, turbidity increases continuously at slower rate up the maximum in $c_{free}(Ca^{2+})$ and $c_{free}(OH^-)$, where another step-like drop occurs (indicated by the arrow in Figure 10a) and no more optical transmission is measured (due to ample precipitation of portlandite).

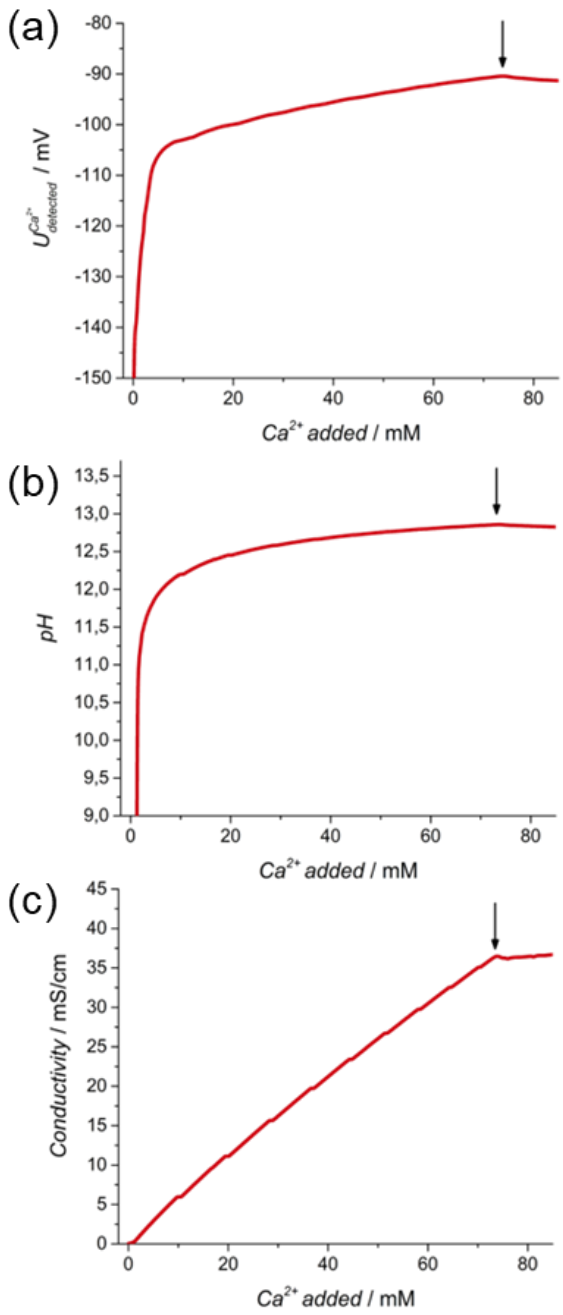

Figure 9. Time-dependent evolution of (a) calcium potential (as measured by an ion-selective electrode), pH value, and (c) conductivity during co-titration of 0.5 M $CaCl_2$ and 1 M NaOH into a solution of poly(acrylic) acid in water (initial volume: 50 mL, initial concentration: 100 ppm) at a dosing rate of 0.2 mL/min each. Arrows indicate the respective maximum in each curve, considered to signify the onset of calcium hydroxide precipitation.

These observations indicate strong interference of PAA during the early and later stages in the pre-nucleation regime. One obvious potential interaction is the direct binding of calcium ions by the polycarboxylate, which may under the given conditions lead to strong association, aggregation, coacervation and even precipitation. To test this, we have performed a reference experiment, in which calcium chloride was titrated into a solution of PAA without simultaneous addition of sodium hydroxide. This titration was performed at a constant pH of 11, as a compromise of being as close as possible to the conditions in the co-titration without actually precipitating portlandite. Moreover, it has been reported that poly(acrylic acid) chains are more or less entirely deprotonated at pH values ≥ 11,[22,63] i.e. the physicochemical properties of the polyelectrolyte and its interaction with calcium ions will not change further when higher pH levels are reached during co-titration. The resulting time-dependent profile (Figure 10a, green curve) indeed shows significant turbidity also in the absence of higher concentrations of hydroxide ions, likely as a consequence of Ca^{2+}/PAA complexation and potentially coacervation, which should remove calcium ions from solution and thus lower the effective supersaturation. However, the decrease in transmittance occurs only at higher calcium concentrations and reaches a minimum at $c_{added}(Ca^{2+}) \approx 20$ mM, subsequent to which the progressive dilution of the solution with respect to PAA leads to dissociation of formed species and partial redissolution. By contrast, turbidity continues increasing in the actual co-titration experiment, which suggests that – in addition to direct interactions with calcium ions – the polycarboxylate also influences portlandite precursors such as ion complexes, clusters and/or ACH particles.

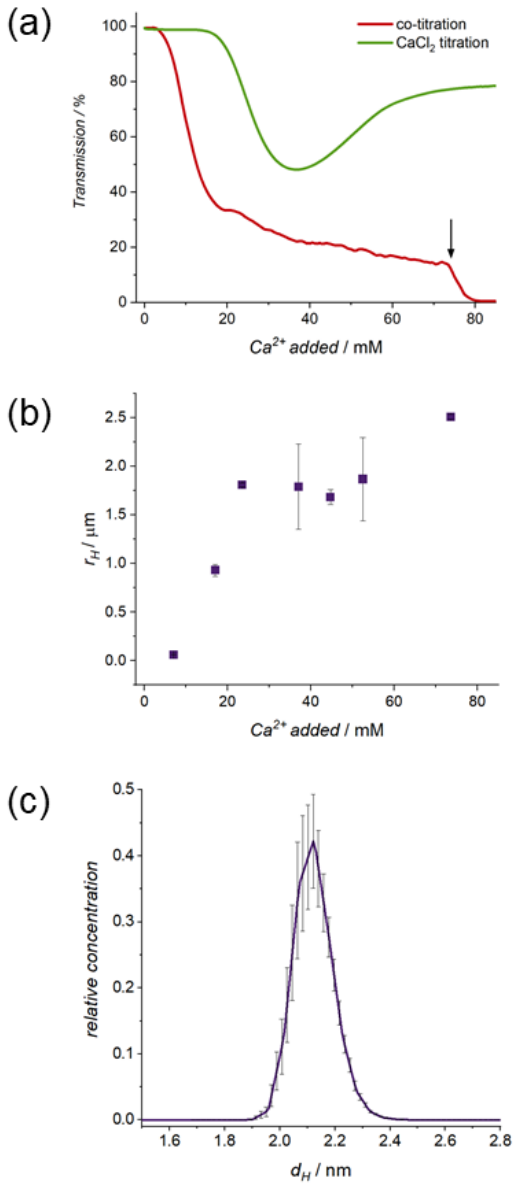

Figure 10. In-situ characterization of species present in solution during the pre- and early post-nucleation stages of portlandite formation under the influence of poly(acrylic acid). (a) Time-dependent evolution of solution transmission during co-titration of 0.5 M $CaCl_2$ and 1 M NaOH into a solution of poly(acrylic) acid in water (initial volume: 50 mL, initial concentration: 100 ppm) at a dosing rate of 0.2 mL/min each (red), as compared to a reference experiment in which $CaCl_2$ was titrated into PAA solution at a constant pH of 11.0 (green). The arrow indicates the final step-like decrease to zero transmission upon crystallization, which coincides with maxima in calcium potential, pH and conductivity shown in Figure 8. (b) Apparent hydrodynamic radii measured by dynamic light scattering for solution aliquots drawn at different stages of the co-titration process. (c) Size distribution obtained from AUC analyses of a sample drawn from the co-titration experiment after addition of 35 mM $CaCl_2$.

Dynamic light scattering (DLS) measurements of solution aliquots collected at different points along the co-titration profile show that quite large species (1-2 µm in hydrodynamic radius) are formed during the initial strong increase in turbidity (Figure 10b). The average size of the scattering species increases up to ca. 3.6 µm after addition of ~22 mM $CaCl_2$, where a plateau is reached without further growth up to $c_{added}(Ca^{2+}) \approx 60$ mM. Around the point of the maxima in all other monitored parameters nucleation ($c_{added}(Ca^{2+}) \approx 76$ mM), the detected average size increases again and soon becomes too high to be measured reliably by DLS. These observations suggest that added poly(acrylic acid) allows amorphous calcium hydroxide particles to be formed, but subsequently controls their growth and/or aggregation behavior and inhibits ultimate transformation into crystalline portlandite; alternatively, the polymer may interfere earlier and stabilize dense liquid droplets, a scenario that cannot be unambiguously confirmed based on the available data. In order to probe potential effects of PAA on the earlier stages of ion complexation and cluster formation, a sample was drawn after addition of ca. 35 mM $CaCl_2$ and analyzed by AUC. The resulting size distribution (Figure 10c) is very similar to that of calcium hydroxide clusters determined under the same conditions in the absence of the polycarboxylate (cf. Figure 4), which suggests that PAA does not affect the nature of the complexes/clusters.

Further insights into the species and processes leading to observed evolution of turbidity and average particle size in the system are provided by cryo-TEM analyses performed at different stages along the co-titration profile (Figure 11). In a sample drawn shortly after the initial drop in solution transmittance (Figure 11a), cryo-TEM images show amorphous nanoparticles that appear to be somewhat larger (100-300 nm in diameter) and more spherical than their counterparts observed during the early stages of the additive-free reference experiment (cf. Figure 5a). These differences in appearance may be considered as (weak) evidence for the

species observed in the presence of polymer at this point to actually be phase-separated complexes (e.g. coacervates) resulting from the direct interaction between calcium ions and PAA. These spherical species are aggregated (possibly bridged to a greater or lesser extent by the polycarboxylate) and have partially fused into larger structures, which seem to become more compact upon further addition of Ca^{2+} and OH^- ions (Figure 11b), possibly due to enhanced incorporation of hydroxide ions into the original Ca^{2+}/PAA complexes (initiating their progressive transformation into polymer-containing ACH). Aggregate sizes observed at this point in cryo-TEM (1-2 µm at $c_{added}(Ca^{2+})$ = 22 mM) are smaller than indicated by concurrent DLS analyses (3-4 µm, cf. Figure 10b), likely because scattering is dominated by the largest agglomerates and the measured hydrodynamic radius includes contributions from hydration shells (and superficially adsorbed polymer). Once the middle of the plateau in DLS particle size is reached ($c_{added}(Ca^{2+})$ = 32 mM), cryo-TEM images reveal most striking structural evolutions in the presence of PAA, which are fundamentally distinct from the reference system: from the compact aggregates of spherical precursors, multiple filamentous structures start to form and extend randomly into the surrounding solution (Figure 11c). These filaments are likewise amorphous (or poorly ordered), account for the large apparent sizes in DLS, and clearly seem to result from the influence of the polycarboxylate on the mineralization process. At this point, we can only speculate about the mechanisms leading to the formation of these unusual structures. In one feasible scenario, PAA forms a more or less continuous layer around the cores of calcium/polymer coacervates and/or polymer-containing ACH, which blocks their further growth as well as re-dissolution. As the inner core dissolves to eventually transform into portlandite, noticeable osmotic pressures may build up across the outer PAA layer.

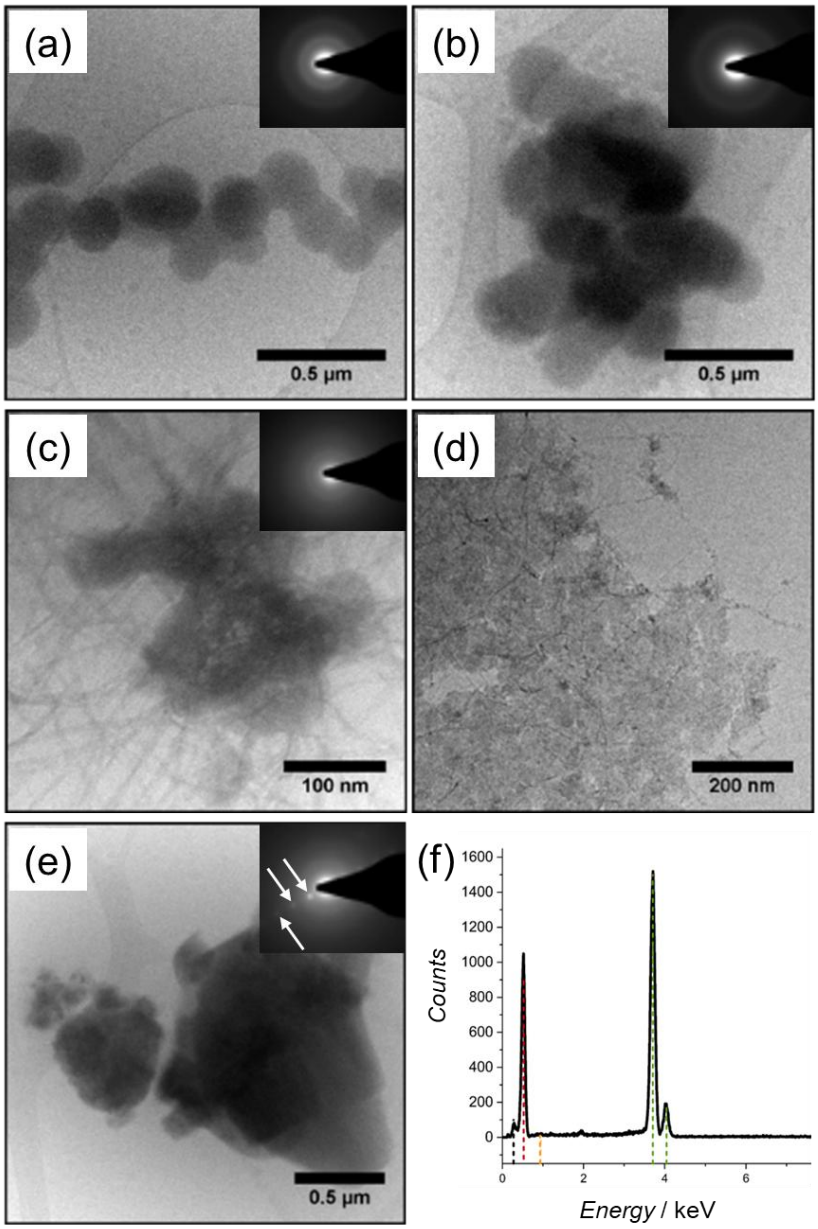

Figure 11. Cryo-TEM images of samples drawn from the co-titration experiment (0.5 M $CaCl_2$ and 1 M NaOH into 50 mL water at 0.2 mL/min) in the presence of poly(acrylic acid) (initial concentration: 100 ppm) after addition of (a) 11, (b) 22, (c) 32, (d) 74 and (e) 79 mM $CaCl_2$. Insets: SAED patterns acquired from the respective shown field of view. White arrows in (e) indicate crystalline reflections in the diffraction images. (f) EDX spectrum collected from the crystals shown in (e), with strong signals from calcium (green) and oxygen (red), weaker signals from copper (orange) and traces of carbon (black) (both originating from the used carbon-filmed copper grids).

Ultimately, this layer would break and release jets of concentrated calcium hydroxide solution into the surrounding medium, where they become solidified under the influence of the organic polymer (forming calcium salts of poly(acrylic acid) at the perimeter of the filaments). This hypothetical mechanism is inspired by the formation of so-called "chemical gardens"[64,65] and the concept of "polymer-induced liquid precursors" (PILP phases),[66] but clearly requires deeper investigations in the present system. In any case, these filamentous structures undergo progressive ripening in the further course of the co-titration: near the maximum in the free concentrations of calcium and hydroxide ions (at $c_{added}(Ca^{2+})$ = 74 mM), filaments can still be distinguished but seem to have partially disintegrated into more continuous domains with granular texture (Figure 11d), which remind of ACH structures proposed to act as growth units for crystalline portlandite via a particle-based mechanism in a recent study.[36] Shortly after the final drop in turbidity and all other monitored solution parameters ($c_{added}(Ca^{2+})$ = 79 mM), crystalline portlandite particles with faceted edges are found by cryo-TEM (Figure 11e), which appear to be less defined than in the absence of PAA (cf. Figure 5f). Nonetheless, EDX spectra acquired at the different sampling times confirm that at least the majority of the observed particles indeed consist of calcium hydroxide (Figure 11f), although we cannot exclude the presence of minor amounts of calcium polyacrylate precipitates.

Differences induced by PAA in the progress and final result of portlandite crystallization from solution are further elucidated by ex-situ characterization, as shown in Figure 12. SEM images of precipitates isolated at different stages of the co-titration procedure reveal ill-defined aggregates with rough surfaces (Figure 12a), which occasionally display crystalline facets (Figure 12b) but generally differ fundamentally from the regular hexagonal crystals observed in the reference experiment without added polymer (cf. Figure 8a-b).

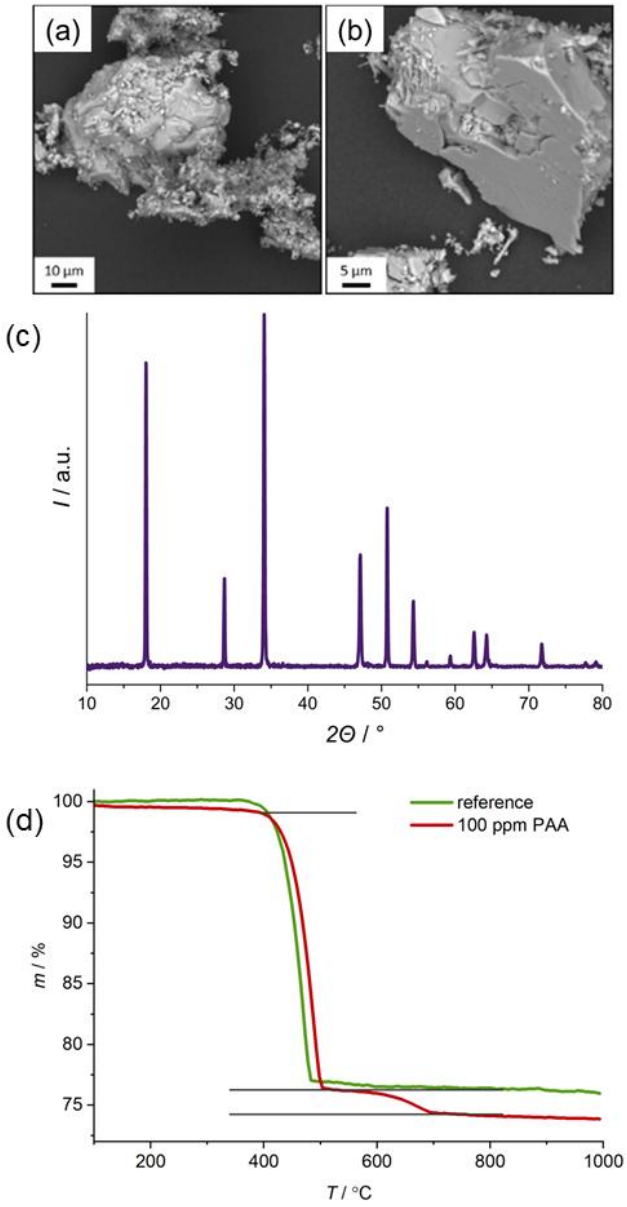

Figure 12. Ex-situ characterization of precipitates formed during a $Ca(OH)_2$ co-titration experiment in the presence of poly(acrylic acid) (initial concentration: 100 ppm). (a-b) SEM image of precipitates isolated after addition of (a) 22 and (b) 32 mM $CaCl_2$, showing irregularly shaped portlandite crystals (scale bars in insets: 2 µm). (c) XRD pattern of powders obtained at the end of the co-titration experiment. All observed reflections can be assigned to crystalline portlandite (ICDD 04-0733),[58] with no signs for the formation of calcium carbonate[59] (due to possible uptake of atmospheric CO_2). (d) TGA data of portlandite powders formed during co-titration experiments in the absence (green line) and presence (red line) of 100 ppm PAA. Note the second step of mass loss for the polymer-containing sample between 500 and 700 °C, caused by decarbonation of $CaCO_3$ formed upon previous heating of poly(acrylic acid) in the presence of calcium species.

Nonetheless, XRD patterns acquired for solid materials extracted at the end of the co-titration procedure confirm portlandite as the only crystalline phase present (Figure 12c). Indeed, no major changes in the position or width of the observed reflections (potentially indicative of lower crystallinity and/or the co-existence of amorphous phases) could be discerned in comparison to diffraction patterns of precipitates formed in the absence of PAA (cf. Figure 8c).

Apart from crystallization kinetics and morphology, the interference of the polycarboxylate with the formation process of portlandite could be traced in three further ways: first, measurements of the PAA concentration in solution before and after the co-titration experiment (via TOC analysis) showed that about 78 % of the polymer were removed from solution upon portlandite precipitation, which corresponds to ca. 1.4 wt% of PAA bound by and/or occluded in the forming inorganic phase. Second, thermogravimetric analyses revealed two stages of mass loss upon heating of precipitates formed in the presence of the polymer (Figure 12d): between 380 and 500 °C, about 23 % of the initial sample weight were removed – mainly due to calcination of portlandite ($M(CaO) / M(Ca(OH)_2) \approx 0.76$),[67] although pure PAA would also be expected to undergo partial decomposition in this temperature range.[68] Further heating resulted in another mass loss of ca. 1.8 % between 500 and 700 °C, which we ascribe to decarbonation of $CaCO_3$ species. Since the precipitates were originally free of any significant amounts of calcium carbonate (as proven by IR spectroscopy, data not shown), the observed thermal behavior must be due to the formation of $CaCO_3$ during heating of polyacrylate in the presence of calcium ions, as reported to occur at temperatures of about 485 °C.[69,70] Thus, the TGA data provide further indirect evidence for the presence of PAA on and/or in the formed portlandite crystals, with absolute amounts that agree reasonably well with the results from TOC-based analyses (i.e. in the range of few percent).

Third, we have investigated the mechanical properties of portlandite powders obtained by co-titration with and without added PAA using nanoindentation. For the additive-free sample, an elastic modulus of ca. 36 GPa was determined, in good agreement with values reported for portlandite in the literature.[71] Interestingly, the presence of the polycarboxylate led to a significant reduction of the *E*-modulus down to ca. 6.5 GPa. This decrease in stiffness suggests that the polymer was incorporated into the bulk of the inorganic phase during crystallization. Assuming that portlandite crystals grow by accretion of preformed (nano)particles,[36] one possible scenario for PAA incorporation is that the polymer adsorbs onto the building units and remains occluded upon collective transformation into a (more or less) continuous crystalline phase.

4. Summary and Conclusions

In this work, we have used a variety of advanced and complementary characterization techniques to probe the early stages of calcium hydroxide crystallization from aqueous solutions. Together with another recent study,[36] our results call a classical mechanism of direct homogeneous nucleation and subsequent growth of crystalline portlandite into serious question and rather suggest a complex multistep pathway involving different precursors, either stable or metastable, before and after actual phase separation, as visualized in Figure 13. In many ways, the observed processes bear fundamental analogy to "non-classical" crystallization schemes reported for calcium carbonate[4-7] and other prominent mineral systems,[9-18] confirming the notion that such multistep pathways are rather the rule than an exception in inorganic mineralization.

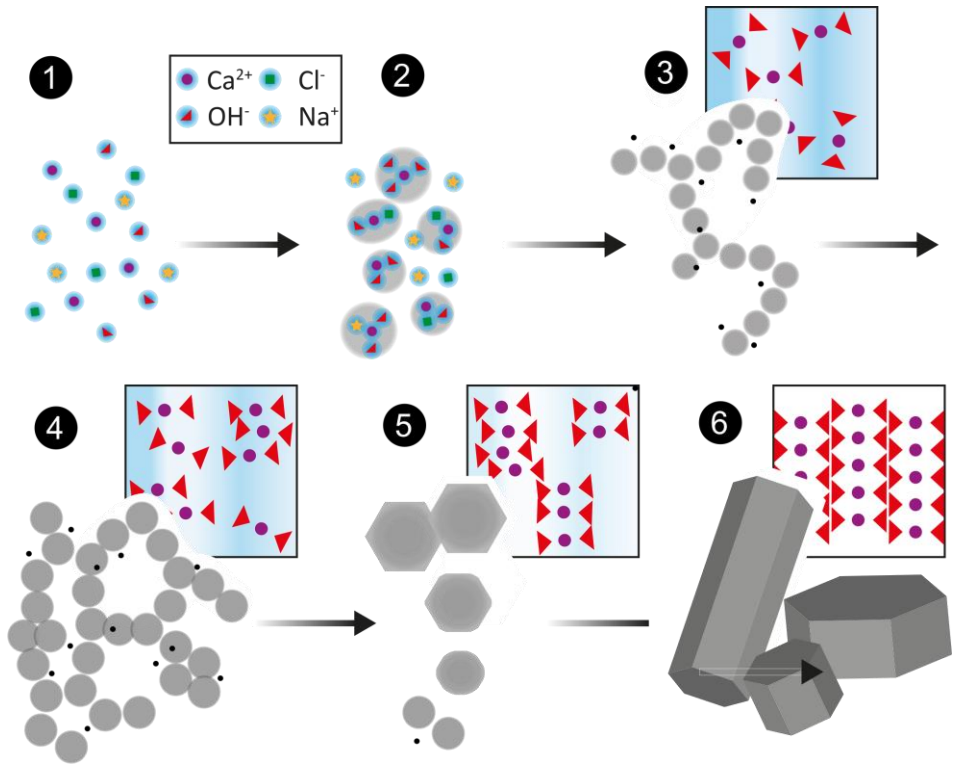

Figure 12. Schematic illustration of the sequential stages underlying the formation of crystalline calcium hydroxide from solution, as envisaged based on the data collected in this work. Stage 1: Single constituent (Ca^{2+} and OH^-) and "spectator" (Na^+ and Cl^-) ions dissolved in water. Stage 2: Ion association into complexes (and clusters) of varying stoichiometry. Stage 3: Coalescence of ion complexes/clusters into larger entities (100-200 nm, presumably of initial liquid-like nature), which immediately start to aggregate into loose networks to minimize interfacial tension. At the same time, smaller species (1-4 nm, indicated by black dots) coexist, as shown by SAXS and AUC, and likely act as building units for the larger structures. Stage 4: Densification of the networks, with concurrent growth and progressive solidification of individual particles into amorphous calcium hydroxide, while primary building units still coexist. Stage 5: Structural reorganization within the aggregated ACH networks and incipient evolution of more ordered matter. Stage 6: Completion of amorphous-to-crystalline transformation and growth of portlandite crystals with regular hexagonal habits. Note that the structures in the different stages are not drawn to relative scale.

The starting point of our study was the development of a robust co-titration procedure, which allowed the evolution of the calcium hydroxide to be monitored all the way from the dissolved ions to the final portlandite crystals. Apart from the fact that ion association produced potentially

nucleation-relevant entities (such as pre-nucleation clusters) early on and already in the undersaturated regime, one particularly striking observation was the continuous variation of stoichiometry of associated species with growing levels of supersaturation – in stark contrast to other systems such as calcium carbonate.[5,47] Indeed, the ratio of bound hydroxide and bound calcium ions was found to gradually increase from ca. 1.3:1 at the beginning of co-titration to almost 2.4:1 at the maximum of $c_{free}(Ca^{2+})$ and $c_{free}(OH^-)$, before ultimately dropping to ~2:1 upon nucleation and growth of crystalline portlandite (as expected). This dynamic evolution renders the identification of nucleation-relevant species as well as the precise mechanisms of nucleation challenging, and certainly warrants further investigation. The complex course of portlandite formation was further probed by a number of powerful in-situ (or close-to-in-situ) techniques, including cryo-transmission electron microscopy, analytical ultracentrifugation, small-angle X-ray scattering and pair-distribution analyses based on high-energy X-ray scattering data. The results obtained from all these studies paint a consistent picture and inevitably confirm a "non-classical" pathway for calcium hydroxide crystallization, in which small nanoclusters (black dots in Figure 13) and amorphous particles and/or droplets (grey circles in Figure 13) play key roles.

In the second part of the work, we have investigated the influence of poly(acrylic acid) – as a model additive for crystallization control – on the newly discovered processes. As expected, the polycarboxylate significantly delayed portlandite formation, i.e., much higher nominal levels of supersaturation were needed to trigger transformation of disordered intermediates towards final crystals (indicated by breakpoints in Figures 9 and 10). Detailed analysis by means of various characterization techniques suggests that the observed delay is caused by interactions of the polymer with (more or less) all detected precursor species – that is, free calcium ions, small

complexes, larger pre-nucleation clusters, as well as amorphous nanoparticles. This list of possible polymer effects is not necessarily complete, as other precursors (e.g., liquid droplets or nanocrystalline building units) may occur and interact with the additive. In any case, binding of the polycarboxylate to the different precursors seems to hamper their transformation into the respective next stage on the energetic ladder down to stable crystals. For example, complexation of calcium ions by PAA competes with Ca^{2+}/OH^- ion association into PNCs, whereas polymer adsorption on ACH particles impedes their aggregation and coalescence. Eventually, the different individual effects add up to strong macroscopic inhibition of crystallization. Notwithstanding this clear influence of the polymer on the progress of portlandite formation, the actual nature of the precursor species does not seem to change fundamentally in the presence of additive. One peculiar difference in the course of ripening is the formation of filamentous structures (cf. Figure 11c) during the transformation of disordered ACH phases to crystalline portlandite, whose composition and origin require further studies. Based on ex-situ analytics, we can conclude that the organic polymer becomes incorporated into the emerging inorganic phase during mineralization and modulates the (mechanical) properties of the resulting solid material – a notion that appears promising in the context of cementitious systems.

In summary, the new insights gained into calcium hydroxide crystallization in the present work and another recent study[36] should have profound implications for any process or application where portlandite plays a significant role – including cement hydration, lime-based mortars, and "nanolimes" for cultural heritage conservation. For example, portlandite precipitation is known to occur during hydration of ordinary Portland cement and thought to influence the dissolution kinetics of anhydrous calcium silicate grains, thereby potentially controlling the overall rate of hydration, especially at the end of the induction period and the main hydration peak.[25,72] The

existence of precursor species such as PNCs or ACH nanoparticles clearly expands the spectrum of possible scenarios to explain experimental observations during cement hydration,[36] and provides new levers to influence the occurring processes. Furthermore, the novel co-titration procedure developed in the present work allows the key stages of portlandite crystallization to be closely monitored and the effects of possible additives to be screened, supporting the design of advanced chemistry solutions for construction applications and beyond in the future.

Acknowledgments

The authors thank Rose Rosenberg (University of Konstanz) for performing AUC measurements, Dr. Michael Laumann and the Electron Microscopy Centre at the University of Konstanz for support during SEM studies, Elisabeth Wagner (BASF SE) for conducting TOC analyses, as well as Ralf Sander and Dr. Tobias Umbach (BASF SE) for carrying out nanoindentation experiments. Access to beamlines ID02 and ID15a at ESRF for SAXS and HEXS experiments through grant numbers ES 526 and ES 608, respectively, and support by ESRF experts is greatly acknowledged.

References

(1) De Yoreo, J. J.; Gilbert, P. U. P. A.; Sommerdijk, N. A. J. M.; Penn, R. L.; Whitelam, S.; Joester, D.; Zhang, H.; Rimer, J. D.; Navrotsky, A.; Banfield, J. F.; Wallace, A. F.; Michel, F. M.; Meldrum, F. C.; Cölfen, H.; Dove, P. M. *Science* **2015**, *349*, aaa6760.

(2) Van Driessche, A. E. S.; Kellermeier, M.; Benning, L. G.; Gebauer, D. *New Perspectives on Mineral Nucleation and Growth: From Solution Precursors to Solid Materials*; Springer International Publishing: Basel, 2017.

(3) Jehannin, M.; Rao, A.; Cölfen, H. *J. Am. Chem. Soc.* **2019**, *141*, 10120.

(4) Wallace, A. F.; Hedges, L. O.; Fernandez-Martinez, A.; Raiteri, P.; Gale, J. D.; Waychunas, G. A.; Withelam, S.; Banfield, J. A.; De Yoreo, J. J. *Science* **2013**, *341*, 885.

(5) Gebauer, D.; Kellermeier, M.; Gale, J. D.; Bergström, L.; Cölfen, H. *Chem. Soc. Rev.* **2014**, *43*, 2348.

(6) Rieger, J.; Kellermeier, M.; Nicoleau, L. *Angew. Chem. Int. Ed.* **2014**, *53*, 12380.

(7) Smeets, P. J. M.; Finney, A. R.; Habraken, W. J. E. M.; Nudelman, F.; Friedrich, H.; Laven, J.; De Yoreo, J. J.; Rodger, P. M.; Sommerdijk, N. A. J. M. *Proc. Natl. Acad. Sci.* **2017**, *114*, E7882.

(8) Avaro, J. T.; Wolf, S. L. P.; Hauser, K.; Gebauer, D. *Angew. Chem. Int. Ed.* **2020**, *59*, 6155.

(9) Habraken, W. J. E. M.; Tao, J.; Brylka, L. J.; Friedrich, H.; Bertinetti, L.; Schenk, A. S.; Verch, A.; Dmitrovic, V.; Bomans, P. H. H.; Frederik, P. M.; Laven, J.; Van der Schoot, P.; Aichmayer, B.; De With, G.; De Yoreo, J. J.; Sommerdijk, N. A. J. M. *Nature Comm.* **2013**, *4*, 1507.

(10) Garcia, N. A.; Innocenti Malini, R.; Freeman, C. L.; Demichelis, R.; Raiteri, P.; Sommerdijk, N. A. J. M.; Harding, J. H.; Gale, J. D. *Cryst. Growth Des.* **2019**, *19*, 6422.

(11) Yang, X.; Wang, M.; Yang, Y.; Cui, B.; Xu, Z.; Yang X. *Phys. Chem. Chem. Phys.* **2019**, *21*, 14530.

(12) Wang, Y. W.; Kim, Y. Y.; Christenson, H. K.; Meldrum, F. C. *Chem. Commun.* **2012**, *48*, 504.

(13) Stawski, T. M.; Van Driessche, A. E. S.; Ossorio, M.; Rodriguez-Blanco, J. D.; Besselink, R.; Benning, L. G. *Nature Comm.* **2016**, *7*, 11177.

(14) Van Driessche, A. E. S.; Stawski, T. M.; Kellermeier, M. *Chem. Geol.* **2019**, *530*, 119274.

(15) Ruiz-Agudo, E.; Burgos-Cara, A.; Ruiz-Agudo, C.; Ibanez-Velasco, A.; Cölfen, H.; Rodriguez-Navarro, C. *Nature Comm.* **2017**, *8*, 768.

(16) Krautwurst, N.; Nicoleau, L.; Dietzsch, M.; Lieberwirth, I.; Labbez, C.; Fernandez-Martinez, A.; Van Driessche, A. E. S.; Barton, B.; Leukel, S.; Tremel W. *Chem. Mater.* **2018**, *30*, 2895.

(17) Baumgartner, J.; Dey, A.; Bomans, P. H. H.; Le Coadou, C.; Fratzl, P.; Sommerdijk, N. A. J. M.; Faivre, D. *Nature Mater.* **2013**, *12*, 310.

(18) Scheck, J.; Wu, B.; Drechsler, M.; Rosenberg, R.; Van Driessche, A. E. S.; Stawski, T. M.; Gebauer, D. *J. Phys. Chem. Lett.* **2016**, *7*, 3123.

(19) Galvan-Ruiz, M.; Hernandez, J.; Banos, L.; Noriega-Montes, J.; Rodriguez-Garcia, M. E.; *J. Mater. Civil Eng.* **2009**, *21*, 694.

(20) Boey, P. L.; Maniam, G. P.; Hamid, S. A. *Chem. Eng. J.* **2011**, *168*, 15.

(21) Surhone, L. M.; Timpledon, M. T.; Marseken, S. F. *Solvay Process*; VDM Publishing, Saarbrücken, 2010.

(22) Büchner, W.; Schliebs, R.; Winter, G.; Büchel, K. H. *Industrial inorganic chemistry*; VCH, Weinheim, 1989.

(23) Wiberg, N.; Holleman, A. F., Wiberg, E.; Fischer, G. *Lehrbuch der Anorganischen Chemie*; Walter de Gruyter, Berlin, 2007.

(24) Locher, F. W. *Zement: Grundlagen der Herstellung und Verwendung*; Verlag Bau und Technik, Düsseldorf, 2000.

(25) Bullard, J. W.; Flatt, R. J. *J. Am. Ceram. Soc.* **2010**, *93*, 1894.

(26) Mindess, S. *The strength and fracture of concrete: The role of the calcium hydroxide*; The American Ceramic Society, Westerville, 2001.

(27) Klein, D. H.; Smith, M. D. *Talanta* **1968**, *15*, 229.

(28) Rodriguez-Navarro, C.; Ruiz-Agudo, E.; Ortega-Huertas, M.; Hansen, E. *Langmuir* **2005**, *21*, 10948.

(29) Rodriguez-Navarro, C.; Hansen, E; Ginell, W. L. *J. Am. Ceram. Soc.* **2005**, *81*, 3032.

(30) Mascolo, G.; Mascolo, M. C.; Vitale, A.; Marino, O. *J. Cryst. Growth* **2010**, *312*, 2363.

(31) Pesce, C.; Pesce, G. L.; Molinari, M.; Richardson, A. *Cem. Concr. Res.* **2021**, *139*, 106524.

(32) Lopez-Arce, P.; Gomez-Villalba, L. S.; Martinez-Ramirez, S.; Alvarez de Buergo, M.; Fort, R. *Powder Technol.* **2011**, *205*, 263.

(33) Ruiz-Agudo, E.; Kudlacz, K.; Putnis, C. V.; Putnis, A.; Rodriguez-Navarro, C. *Environ. Sci. Technol.* **2013**, *47*, 11342.

(34) Rodriguez-Navarro, C.; Burgos-Cara, A.; Elert, K.; Putnis, C. V.; Ruiz-Agudo, E. *Cryst. Growth Des.* **2016**, *16*, 1850.

(35) Rodriguez-Navarro, C.; Ruiz-Agudo, E. *Pure Appl. Chem.* **2018**, *90*, 523.

(36) Rodriguez-Navarro, C.; Burgos-Cara, A.; Di Lorenzo, F.; Ruiz-Agudo, E.; Elert, K. *Cryst. Growth Des.* **2020**, *20*, 4418.

(37) Cölfen, H.; Mann, S. *Angew. Chem. Int. Ed.* **2003**, *42*, 2350.

(38) Song, R. Q.; Cölfen, H. *Cryst. Eng. Comm.* **2011**, *13*, 1249.

(39) Guinier, A.; Fournet, G. *Small-angle scattering of X-rays*; John Wiley & Sons, Inc., New York, 1955.

(40) Bergmann, R. B.; Bill, A. *J. Cryst. Growth* **2008**, *310*, 3135.

(41) Ilavsky, J.; Jemian, P. R. *J. Appl. Crystallogr.* **2009**, *42*, 347.

(42) Planken, K. L.; Cölfen, H. *Nanoscale* **2010**, *2*, 1849.

(43) Juhas, P.; Davis, T.; Farrow, C. L.; Billinge, S. J. L. *J. Appl. Crystallogr.* **2013**, *46*, 560.

(44) Lamer, V. K.; Dinegar, R. H. *J. Am. Chem. Soc.* **1950**, *72*, 4847.

(45) Rodriguez-Navarro, C.; Suzuki, A.; Ruiz-Agudo, E. *Langmuir* **2013**, *29*, 11457.

(46) Kellermeier, M.; Picker, A.; Kempter, A.; Cölfen, H.; Gebauer, D. *Adv. Mater.* **2014**, *26*, 752.

(47) Gebauer, D.; Völkel, A.; Cölfen, H. *Science* **2008**, *322*, 1819.

(48) Stawski, T. M.; Besselink, R.; Chatzipanagis, K.; Hövelmann, J..; Benning, L. G.; Van Driessche, A. E. S. *J. Phys. Chem. C* **2020***, 124,* 8411.

(49) Haynes, W. M. *Handbook of Chemistry and Physics*; CRC Press: Boca Raton, 2014.

(50) Kelly, D. J.; Clark, N.; Zhou, M.; Gebauer, D.; Gorbachev, R. V.; Haigh, S. J. *Adv, Mater.* **2021**, *33*, 2100668.

(51) Desgranges, L; Grebille, D; Calvarin, G; Chevrier, G; Floquet, N; Niepce, J. C. *Acta Crystallogr. B* **1983**, *49*, 812.

(52) Soper, A. K. *ISRN Phys. Chem.* **2013**, 279463.

(53) Zobel, M.; Neder, R. B.; Kimber, S. A. J. *Science* **2015**, *347*, 292.

(54) Thomä, S. L. J.; Krauss, S. W.; Eckardt, M.; Chater, P.; Zobel, M. *Nature Comm.* **2019**, *10*, 995.

(55) Zobel, M. *Acta Cryst. A*, **2016**, *72*, 621.

(56) Lozano, A.; Fernandez-Martinez, A.; Ayora, C.; Di Tommaso, D.; Poulain, A.; Rovezzi, M.; Marini, C. *Environ. Sci. Technol.*, **2019**, *53*, 19.

(57) Harutyunyan, V. S.; Kirchheim, A. P.; Monteiro, P. J. M.; Aivazyan, A. P.; Fischer, P. *J. Mater. Sci.* **2009**, *44*, 962.

(58) Henderson, D. M.; Gutowsky, H.S. *Am. Mineral.* **1962**, *47*, 1231

(59) Neira-Carrillo, A.; Acevedo, D. F.; Miras, M. C.; Barbero, C. A.; Gebauer, D.; Cölfen, H; Arias, J. L. *Langmuir*, **2008**, *24*, 12496

(60) Gebauer, D.; Cölfen, H.; Verch, A.; Antonietti, M. *Adv. Mater.* **2009**, *21*, 435.

(61) Ruiz-Agudo, C.; Ruiz-Agudo, E.; Burgos-Cara, A.; Putnis, C. V.; Ibanez-Velasco, A.; Rodriguez-Navarro, C.; Putnis, A. *Cryst. Eng. Comm.* **2016**, *18*, 2830.

(62) Jiang, S.; Cao, Y.; Li, S.; Pang, Y.; Sun, Z. *J. Cryst. Growth* **2021**, *557*, 125991.

(63) Swift, T.; Swanson, L.; Geoghegan, M.; Rimmer, S. *Soft Matter* **2016**, *12*, 2542.

(64) Kellermeier, M.; Glaab, F.; Melero-Garcia, E.; Garcia-Ruiz, J. M. *Methods in Enzymology* **2013**, *532*, 225.

(65) Barge, L. M.; Cardoso, S. S. S.; Cartwright, J. H. E.; Cooper, G. J. T.; Cronin, L.; De Wit, A.; Doloboff, I. J.; Escribano, B.; Goldstein, R. E.; Haudin, F.; Jones, D. E. H.; Mackay, A. L.; Maselko, J.; Pagano, J. J.; Pantaleone, J.; Russell, M. J.; Sainz-Diaz, C. I.; Steinbock, O.; Stone, D. A.; Tanimoto, Y.; Thomas, N. L. *Chem. Rev.* **2015**, *115*, 8652.

(66) Olszta, M. J.; Odom, D. J.; Douglas, A. P.; Gower, L. B. *Connect. Tissue Res.* **2003**, *44*, 326.

(67) Scrivener, K.; Snellings, R.; Lothenbach, B. *A practical guide to microstructural analysis of cementitious materials*, CRC Press, Boca Raton, 2016.

(68) Tai, Z.; Yang, J.; Qi, Y.; Yan, X.; Xue, Q. *RSC Adv.* **2013**, *3*, 12751.

(69) McNeill, I. C.; Sadhegi, S. M. T. *Polym. Degrad. Stabil.* **1990**, *30*, 267.

(70) Garay, A. C.; Heck, V.; Zattera, A. J.; Souza, J. A.; Amico, S. C. *J. Reinf. Plast. Comp.* **2011**, *30*, 1213.

(71) Laugesen, J. L. *Cem. Concr. Res.* **2005**, *35*, 199

(72) Scrivener, K. L.; Juilland, P.; Monteiro, P. J. M. *Cem. Concr. Res.* **2015**, *78*, 38.

Corresponding Author

* Dr. Matthias Kellermeier (E-Mail: matthias.kellermeier@basf.com, Phone: (+49) (0)621 60 43388, Postal Address: Material Science, BASF SE, Carl-Bosch-Strasse 38, D-67056 Ludwigshafen, Germany)

Author Contributions

The manuscript was written through contributions of all authors. All authors have given approval to the final version of the manuscript.